Modelling Dayside and Nightside Reconnection Rates for the Expanding/Contracting Polar Cap Paradigm

Anh-Nguyet Lise Nguyen

Thesis submitted for the degree of
Master in Space Physics and Technology
60 credits

Department of Physics
Faculty of mathematics and natural sciences

UNIVERSITY OF OSLO

Spring 2021

Modelling Dayside and Nightside Reconnection Rates for the Expanding/Contracting Polar Cap Paradigm

Anh-Nguyet Lise Nguyen

Modelling Dayside and Nightside Reconnection Rates for the Expanding/Contracting Polar Cap Paradigm

http://www.duo.uio.no/

Printed: Reprosentralen, University of Oslo

Abstract

Space weather can cause disturbances in Global Navigation Satellite Systems (GNSS) signals at high latitudes predominantly in the form of phase scintillations. These scintillations are mainly caused by polar cap patches, islands of elevated plasma density, being dragged across the polar cap from the dayside into the nightside auroral oval by ionospheric convection that arise due to solar wind-magnetosphere coupling. A previous model has been built on the expanding/contracting polar cap paradigm (ECPC) to estimate patch formation and propagation in order to predict scintillations in GNSS at high latitudes. The model simulates the ionospheric convection that transports the polar cap patches from the dayside to the nightside based on time series of solar wind-magnetosphere coupling at the magnetopause and in the magnetotail. In their paper, these reconnection rates were somewhat arbitrarily based on Super Dual Aurora Network (SuperDARN) estimates of the cross polar cap potential. In this study we propose and develop a statistical method to generate synthetic reconnection rates to be used in an ECPC ensemble model. The synthetic reconnection rates are generated 90 minutes ahead of time from an instantaneous IMF Bz measurement, and are based on historical values of reconnection rates derived from Active Magnetosphere and Planetary Electrodynamics Response Experiment (AMPERE) data. The synthetic reconnection rate values are generated by sampling from gamma distributions fitted to the historical data. We find that the mean values of the synthetic reconnection rates are able to convincingly replicate the means of the actual reconnection rates.

Acknowledgements

I acknowledge use of NASA/GSFC's Space Physics Data Facility's OMNIWeb (or CDAWeb or ftp) service and OMNI data, and Iridium-derived data products from the AMPERE team and the AMPERE Science Center.

I am grateful to my supervisor Lasse Clausen for believing in me and always pushing me to improve, and for his incredibly detailed and thorough feedback. You helped elevate my work to a level I did not believe I could achieve. I would also like to thank my co-supervisor Anna Fæhn Follestad for her help and guidance, and for providing a solid foundation on which I could base my project.

I would like to thank my fellow classmates Aksel, Amund, Michael, Saida and Sean for their invaluable support and friendship throughout this turbulent year. Your companionship and willingness to help made this year a lot less lonely and I cannot imagine what it would have been like without you. You are the best classmates I could ever dream of having.

Lastly, I would like to express my gratitude towards my significant other Bernhard, my sister Sandra and all my friends for keeping me motivated and supporting me in times of doubt. Thank you for always cheering me on and for your unwavering confidence and trust in me. I truly could not wish for better people to surround myself with.

Contents

Chapter 1

Introduction

Space weather is used to refer to phenomena that arise from conditions in the Sun that are able to influence the magnetosphere, thermosphere and ionosphere of the Earth [e.g. *Gold*, 1959]. These phenomena can cause disturbances in satellite signals in the form of rapid fluctuations in the amplitude or phase of the signal travelling through the ionosphere, degrading the signal. These fluctuations are commonly referred to as scintillations, and are caused by plasma irregularities in the ionosphere [*Aarons*, 1993]. As modern technology is growing increasingly reliant on Global Navigation Satellite Systems (GNSS) with their wide range of applications, the importance of understanding and eventually forecasting space weather phenomena like scintillations is increasing. Several studies have found that scintillations occur frequently at high latitudes and in the equatorial region [e.g. *Fremouw et al.*, 1978; *Basu et al.*, 1988], with phase scintillations as the predominant type of scintillation in the Global Positioning System (GPS) at high latitudes [*Spogli et al.*, 2009; *Prikryl et al.*, 2011]. Strong phase scintillations at high latitudes occur more frequently near magnetic midnight due to the transportation of islands of high plasma density across the polar cap [*Jin et al.*, 2015, 2016] towards the nightside. These islands of elevated plasma density are often referred to as polar cap patches and are typically at least two times as dense as the background plasma *Crowley* [1996]. Polar cap patches are created inside the magnetic dayside cusp and transported towards magnetic nightside by polar ionospheric convection that arise due to coupling between the interplanetary magnetic field (IMF) and the Earth's magnetic field [e.g. *Oksavik et al.*, 2010], eventually transforming into blobs after entering the nightside auroral oval and causing scintillations [*Crowley et al.*, 2000].

Fæhn Follestad et al. [2019] built a prediction model to forecast the formation and propagation of polar cap patches given satellite measurements of the IMF at the first Lagrange point. By predicting the patch formation, trajectory and subsequently entry into the auroral oval, they were able

to predict scintillations in GNSS signals at high latitudes. Their model is based on the Expanding/Contracting Polar Cap Paradigm (ECPC) model initially suggested by *Freeman* [2003], with nightside reconnection gap modified according to *Milan* [2013] and *Walach et al.* [2017]. The model builds on the concept of expanding and contracting polar caps in response to IMF conditions and solar wind-magnetosphere coupling as introduced by *Siscoe and Huang* [1985], *Lockwood and Cowley* [1992] and *Cowley and Lockwood* [1992]. The expansion of the polar cap is related to reconnection between the IMF and the geomagnetic field on the dayside and the resulting increase in open magnetic flux in the magnetosphere, whereas the contraction is caused by reconnection in the magnetotail. This process will be further elaborated on in the Theory chapter. *Fæhn Follestad et al.* [2019] in their study used time series of dayside and nightside reconnection based on cross polar cap potentials derived from measurements of the Super Dual Aurora Network (SuperDARN), with the dayside and nightside distributions somewhat arbitrarily decided. The aim of this study is to propose and develop a new method for statistically producing future time series of reconnection rates given an initial value of the IMF. New time series of dayside and nightside reconnection rates are predicted based on statistical distributions of historical data of reconnection rates. The reconnection rates used in this study are derived from the open magnetic flux in the R1 current oval as presented in *Clausen et al.* [2012] and *Clausen et al.* [2013b] using measurements from the Active Magnetosphere and Planetary Electrodynamics Response Experiment (AMPERE). Using our method, new series of future reconnection rates can be repeatedly generated to be used in *Fæhn Follestad et al.* [2019]'s ECPC model, yielding a more statistical forecast of patch formation and propagation. This study is part of an effort to develop a scintillation forecast based on instantaneous IMF conditions using the ECPC model. Successfully modelling reconnection rate series would allow us to more accurately forecast patches and scintillations.

Chapter 2

Theory

2.1 The interplanetary magnetic field and magnetosphere

The interplanetary magnetic field (IMF) is the extended component of the magnetic field of the solar corona dragged into the solar system by the solar wind. The solar wind plasma flow is frozen-in to the magnetic field lines and cannot diffuse through it, i.e. the magnetic field lines are frozen to the plasma and is dragged along with it [*Owens and Forsyth*, 2013].

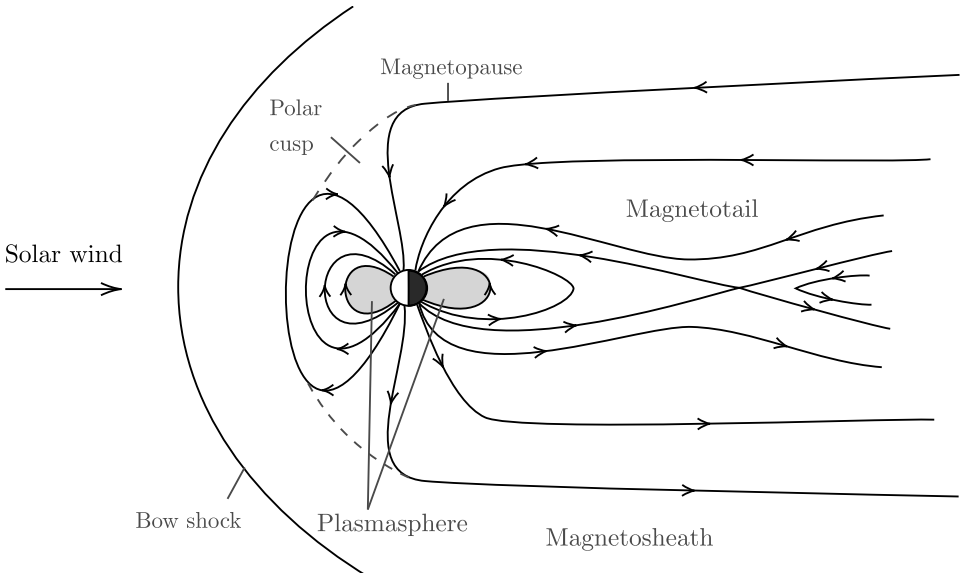

Figure 2.1: Illustration of the noon-midnight cross section of the terrestrial magnetic field. Distances and objects not to scale. [After *Russell*, 1972]

Figure 2.1 shows an illustration of Earth's magnetic field confined by the solar wind flow. As the solar wind travels towards the Earth, it is deflected

and decelerated by the bow shock [*Russell*, 1972; *Russell et al.*, 2016]. The shocked solar wind enters the magnetosheath, which is the region between the bow shock and magnetopause. The magnetopause is the area at which the pressure of the solar wind and the pressure of the magnetic field are balanced, compressing the terrestrial magnetic field. It is considered to be the boundary between the magnetosphere and the solar wind plasma. The plasma is able to enter the Earth's ionosphere at high latitudes through the polar cusp. The magnetotail is the extension of the magnetosphere on the nightside.

2.2 Dungey cycle

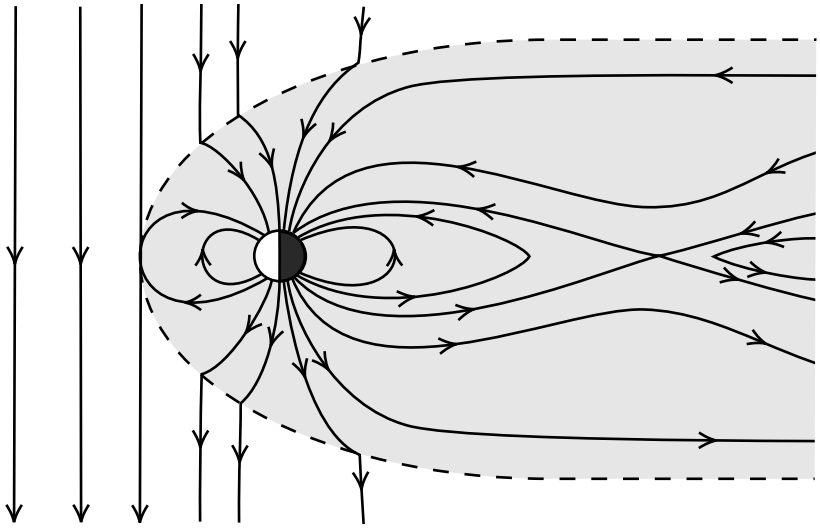

Figure 2.2: Illustration of the Dungey cycle. The southward IMF and the magnetosphere reconnect at the magnetopause. The open field lines are accelerated towards the nightside where they eventually reconnect in the magnetotail. Distances and objects not to scale. [After *Russell et al.*, 2016]

Dungey [1961] proposed magnetic reconnection between the IMF and the Earth's magnetosphere on the dayside and the magnetotail as the main driver for the so-called Dungey cycle. This cycle is illustrated in Figure 2.2. When the IMF is directed southwards, i.e. the IMF Bz-component is negative, we have coupling between the IMF and the geomagnetic field at the magnetopause. The IMF and the magnetosphere are directly connected as open magnetic field lines, thus connecting the solar wind to the Earth's ionosphere. The boundary between the open field lines and the closed field lines is called the open-closed field line boundary (OCB), with the polar cap being defined as the area enclosed by this boundary. The polar cap

expands as a result of the opening of previously closed field lines during dayside reconnection and we have an increase in open magnetic flux [*Siscoe and Huang*, 1985]. The open field lines are accelerated anti-sunward towards the magnetotail and dragged across the polar cap, and the magnetic flux is added to the tail. The open field lines eventually reconnect and close in the tail. The nightside reconnection leads to contraction of the polar cap and the magnetotail releases the stored magnetic energy [*Siscoe and Huang*, 1985; *Cowley and Lockwood*, 1992; *Lockwood and Cowley*, 1992].

The resulting auroral phenomena in the Earth's ionosphere and magnetosphere are collectively referred to as a substorm. These phenomena can lead to e.g. disturbances in the geomagnetic field, aurora and enhancement of ionospheric convection patterns. The substorm sequence can generally be divided into the growth phase, expansion phase and recovery phase [*McPherron et al.*, 1973]. The growth phase occurs when the southward IMF Bz and the magnetosphere initially reconnect at the magnetopause (dayside reconnection), followed by the onset of tail reconnection, triggering the expansion phase and a rapid expansion of the aurora and increasing disturbances in the geomagnetic field at the Earth's surface. The substorm eventually enters the recovery phase as nightside reconnection dominates, closing the open field lines and the geomagnetic disturbances gradually decrease [e.g. *McPherron et al.*, 1973; *Kamide et al.*, 1996; *Partamies et al.*, 2013]. The polar cap contracts back to its initial size [*Lockwood and Cowley*, 1992].

The expanding-contracting polar cap paradigm (ECPC) describes the expansion and contraction of the polar cap driven by dayside and nightside reconnection rates, where dayside reconnection drives polar cap expansion and subsequent nightside reconnection drives polar cap contraction, as suggested by *Cowley and Lockwood* [1992]; *Lockwood and Cowley* [1992]. The expansion and subsequent contraction of the polar cap due to magnetic reconnection during a substorm leads to a corresponding change in open magnetic flux, which can be expressed as the difference in dayside and nightside magnetic reconnection rates [*Siscoe and Huang*, 1985],

$$\frac{dF_{PC}}{dt} = \Phi_D - \Phi_N \tag{2.1}$$

where F_{PC} is the open magnetic flux in the polar cap, Φ_D is the dayside reconnection rate and Φ_N is the nightside reconnection rate and nightside reconnection. The ECPC also provides an understanding of the large-scale ionospheric convection patterns based on conditions in the solar wind. The Birkeland currents are a set of geomagnetic field-aligned currents connecting the ionosphere and the magnetosphere, also referred to as field-aligned currents (FACs), and are closely related to auroral phenomena and convection [*Iijima and Potemra*, 1976]. The FAC strengths have been shown to be strongly correlated with the dayside reconnection rate *Coxon et al.* [2014], with a strengthening of the currents occurring during substorms.

The currents typically form two concentric rings in the ionosphere at high latitudes, with the inner poleward region 1 (R1) ring and the outer equatorward region 2 (R2) ring. The R1 currents flow into the ionosphere on the dawn side and out on the dusk side, while the R2 current flow is reversed to the R1 current and flows into the ionosphere on the dusk side and out of the ionosphere on the dawn side [*Iijima and Potemra*, 1978]. The dayside and nightside reconnection lead to enhanced FACs and a horizontal electric field, which sets up an $\vec{E} \times \vec{B}$-drift of plasma, where $\vec{B}$ is the magnetic field and $\vec{E}$ is the electric field *Cowley* [2000]. This drift follows a twin-cell convection pattern, a simplified illustration of which is shown in Figure 2.3 for the northern hemisphere. The plasma flows from the magnetic dayside across the polar cap to the nightside. The R1 currents connect the ionosphere to the magnetopause and magnetotail, while the R2 currents connect to the ring current in the inner magnetosphere [*Cowley*, 2000]. The R1 and R2 currents connect in the high latitude ionosphere through horizontal currents. *Clausen et al.* [2012] showed that the FACs expand and contract latitudinally in a manner that is consistent with the expansion and contraction of the polar cap associated with the Dungey cycle. *Clausen et al.* [2013b] developed a method to calculate the open magnetic flux F_{PC} from the inner poleward ring size and location. This method is explained in more detail in chapter 3.

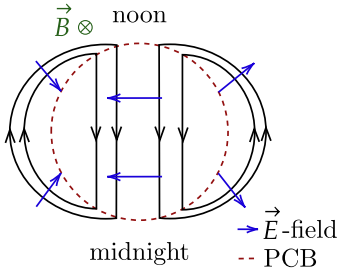

Figure 2.3: Illustration of the ionospheric two-cell convection pattern in the northern hemisphere driven by $\vec{E} \times \vec{B}$-drift during dayside and nightside reconnection. The solid lines represent the plasma flow, while the dashed line represents the polar cap boundary (PCB). Simplified from *Cowley and Lockwood* [1992]; *Cowley* [2000].

Polar cap patches, areas of enhanced plasma density at least twice the density of surrounding plasma [*Crowley*, 1996], form in the cusp region on the magnetic dayside. The dynamics behind patch formation are not yet fully understood [*Zhang et al.*, 2011]. Dayside reconnection and subsequent nightside reconnection give rise to the ionospheric twin-cell convection, pulling polar cap patches across the polar cap from the dayside towards the nightside [*Weber et al.*, 1984; *Oksavik et al.*, 2010]. Upon exiting the polar cap and entering the nightside auroral oval, the polar cap patches transform into auroral blobs and cause scintillations [*Jin et al.*, 2014]. *Fæhn Follestad et al.* [2019] built a prediction model based on ECPC to forecast polar cap patch formation and propagation as part of an effort to develop a scintillation forecast. As dayside reconnection and nightside reconnection are the main drivers behind the resulting expansion and contraction of the polar cap in ECPC [*Cowley and Lockwood*, 1992; *Lockwood*

and Cowley, 1992], being able to model these rates would contribute to a more accurate forecast of patch formation and propagation. However, separating the dayside and nightside reconnection rates has proved challenging. The cross polar cap potential (CPCP) is considered instead, as it reflects the rate of magnetic flux transfer that is coupled into the geomagnetic field during solar wind-magnetosphere coupling [*Bristow et al.*, 2004]. Assuming a circular polar cap, it is related to the reconnection rates as

$$\Phi_{PC} = \Phi_v + \frac{1}{2}(\Phi_D + \Phi_N), \tag{2.2}$$

where Φ_{PC} is the CPCP, Φ_D is the dayside reconnection rate and Φ_N is the nightside reconnection rate and Φ_v is the potential due to any viscous-like interactions [*Lockwood and Cowley*, 1992]. Various methods to estimate the CPCP have been developed [e.g *Shepherd and Ruohoniemi*, 2000; *Gao*, 2012]. *Fæhn Follestad et al.* [2019] in their ECPC model use the CPCP derived by the Super Dual Aurora Network (SuperDARN) to estimate the dayside and nightside reconnection rates as

$$\Phi_{PC} = \frac{1}{2}(\Phi_D + \Phi_N). \tag{2.3}$$

To separate the dayside and nightside reconnection rates, the dayside reconnection Φ_D was assumed to be 10 kV higher than the CPCP Φ_{PC} during the substorm growth phase, while the nightside reconnection rate Φ_N is 10 kV lower. The nightside reconnection rate was then assumed to dominate the rest of the substorm duration. In this study we propose a new method to model series of dayside and nightside reconnection rates given an initial IMF Bz value to be used with ECPC. We use historical data of magnetic flux to derive reconnection rates, from which we generate synthetic reconnection rates 90 minutes into the future given an initial IMF Bz value based on statistical distributions of the historical rates. By repeatedly running the ECPC model as implemented by *Fæhn Follestad et al.* [2019] using new series of synthetic rates as an ensemble model, it is possible to obtain a more statistical forecast of future patch propagation given an instantaneous IMF Bz measurement.

Chapter 3

Data and measurements

The dataset consists of OMNI measurements of the interplanetary magnetic field strengths in GSM coordinates from a period of time between 05:00 UT 1st of January 2010 and 23:55 UT 31st of August 2017, in addition to corresponding values for the total R1 Birkeland current and open magnetic flux in the northern and southern hemisphere. The OMNI dataset consists of IMF measurements from satellites outside the magnetosphere that have been time-shifted to the bow shock [*King and Papitashvili*, 2005]. The R1 Birkeland current and open magnetic flux data were derived from current density measurements from the Active Magnetosphere and Planetary Electrodynamics Response Experiment (AMPERE) by *Clausen et al.* [2012], the derivation of which will be explained later in the chapter. The IMF Bz and By strength measurements were originally extracted from NASA/GSFC's OMNI 1-minute resolution dataset. The resolution was subsequently altered to two minutes to match the resolution of the magnetic flux data. Due to longer periods of missing measurements, we only have approximately 1.8 millions time points of measurements rather than the 2 million we would have had during the full period.

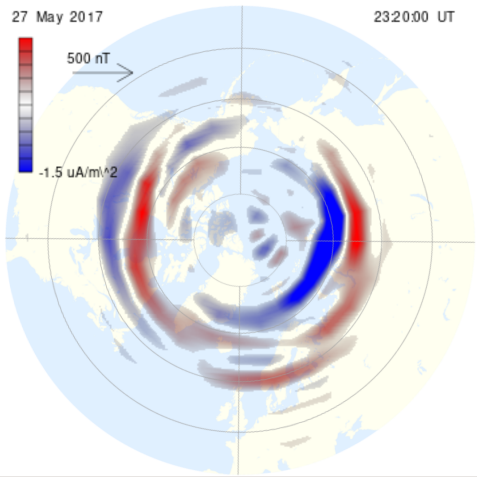

Figure 3.1: AMPERE current densities from 23:20 UT 27 May 2017. The densities in red are the upward FACs and the blue are the downward FACs.

The Iridium® constellation consists of over 66 satellites in low altitude

circular polar orbits in six evenly spaced orbital planes. Each satellite carries an engineering magnetometer, providing in-situ measurements of the geomagnetic field. *Anderson et al.* [2000]; *Waters et al.* [2001] showed that it was possible to estimate the large scale field-aligned currents (FACs) by using these measurements to map global magnetic perturbations caused by the FACs. However, due to latitude spacing of the satellites and the time resolution at which the data was telemetered to the ground, at least an hour of data was required to obtain only a crude estimate of magnetic disturbances [*Coxon et al.*, 2018; *Korth et al.*, 2010]. The National Science Foundation funded the Active Magnetosphere and Planetary Electrodynamics Response Experiment (AMPERE) to resolve this problem by implementing software on the satellites to downlink measurements at standard rate (19.44 s intervals) or high rate (2.16 s intervals) [*Anderson et al.*, 2014]. The radial current densities can then be estimated every 10 minutes, enabling us to observe the dynamics and small scale features of the R1 and R2 current densities. Figure 3.1 shows an example of upward and downward field-aligned current densities found by AMPERE. The R1 and R2 current systems typically form two concentric rings, with the inner poleward current flowing into the ionosphere on the dawn side and out on the dusk side. The equatorward R2 current flow is reversed to the R1 current and flows out of the ionosphere on the dawn side and into the ionosphere on the dusk side [*Iijima and Potemra*, 1978]. This pattern can also be seen in the figure. *Clausen et al.* [2012] used the AMPERE current densities to estimate the location and size of the maximum R1 currents, which they termed the R1 oval. They argued that the R1 oval size can be used to describe the accumulation of open magnetic flux in the magnetosphere, as the change in size of the oval reflects the expansion and contraction of the polar cap during substorms. The R1 Birkeland currents in our dataset are derived from the maximum R1 currents along this oval. *Clausen et al.* [2013a] showed that the R1 oval could be used as a proxy for the open-closed field line boundary (OCB), as it is on average located 1° equatorward of particle precipitation boundaries associated with the OCB determined by the Defense Meteorological Satellite Program (DMSP). By shifting the R1 oval 1° poleward we obtain an estimate for the location of the OCB. *Clausen et al.* [2013b] were able to estimate the amount of open magnetic flux inside the magnetosphere by integrating the vertical component of the International Geomagnetic Reference Field over the area enclosed by the OCB. The open magnetic flux we use in this study has been derived according to this method.

Chapter 4

Method

We want to model time series of the dayside and nightside reconnection rates using a given initial value of the Z-component of the IMF, as this component is what predominantly determines the dynamics of dayside reconnection in the magnetosphere [*Arnoldy*, 1971; *Cowley and Lockwood*, 1992]. By generating new time series of reconnection rates given an instantaneous IMF Bz measurement, we can use these time series to model future ionospheric convection based on the ECPC paradigm *(note: ECPC paradigm will be explained in introduction and/or theory)*. To achieve this we want to find and sample from suitable probability distributions representing the reconnection rates. Because our IMF Bz measurements cover a wide range of values, we first divide them into ten bins, with each bin containing the same amount of IMF Bz measurements. For each IMF Bz bin, we will consider the dayside and nightside reconnection rates starting from when the IMF Bz measurement occurred to 90 minutes after. Each time point, given an IMF Bz bin, will have a dayside and a nightside reconnection rate distribution respectively. To generate new rates with an initial IMF value, we for each time point sample a reconnection rate value from the corresponding distribution until we reach 90 minutes, with each IMF Bz interval having its own set of dayside and nightside distributions.

4.1 Obtaining the dayside and nightside reconnection rates

Our dataset does not contain explicit numbers for the dayside and nightside magnetic reconnection rates, meaning that we need to find a way to derive them from the data that we do have. The data contains estimates of the amount of open magnetic flux in the polar cap of the northern and southern hemispheres respectively. From Equation 2.1, we see that the change in open magnetic flux can be expressed as the nightside reconnection rate subtracted from the dayside reconnection rate. This means that we can use the mag-

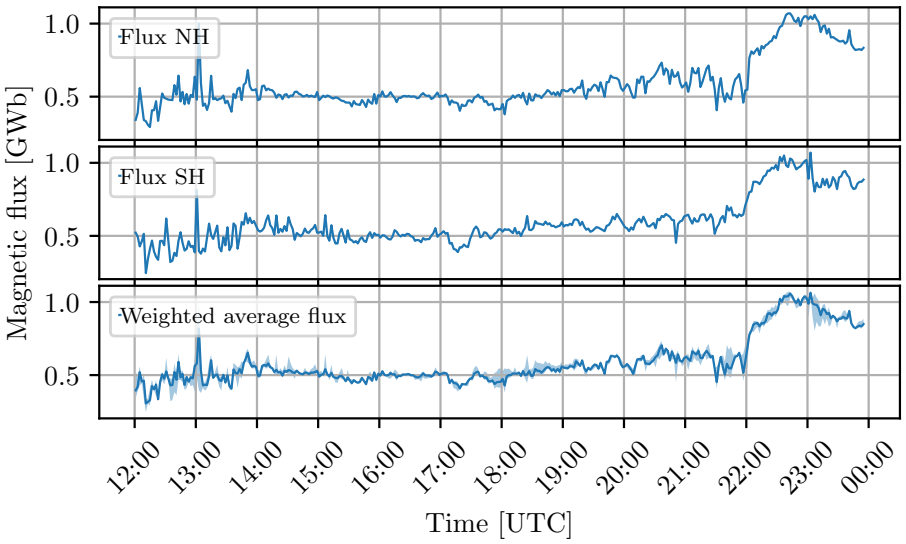

Figure 4.1: The plot shows an example of the magnetic flux in the northern hemisphere (NH) and southern hemisphere (SH), as well as the weighted average flux of the two. The lowest plot also shows the filled in area between the upper and lower envelopes of the NH and SH fluxes. The hemisphere with the stronger R1 current density was weighed more heavily at each time point.

netic flux to estimate the reconnection rates. Rather than deriving one series of dayside and nightside reconnection rates from two separate magnetic flux time series, we can combine the open magnetic flux in the northern and southern hemispheres into one by performing a weighted average. When obtaining the open flux estimates using R1 current densities found by *Clausen et al.* [2012], they observed that the current densities obtained from periods of weaker AMPERE current densities contained larger errors while stronger current densities generally had smaller errors. Subsequently, the errors in the open magnetic flux derived from these current densities should be larger for weaker current densities and smaller for stronger current densities. We choose to do a weighted average of the open flux in the northern and southern polar caps, with the flux derived from the stronger current being weighted at 0.7 and the flux derived from the weaker current weighted at 0.3. These weights were chosen somewhat arbitrarily. An example of the resulting flux can be seen in Figure 4.1, along with the upper and lower envelopes of the NH and SH flux values. We observe that while the general shapes of the two flux values are preserved in the weighted average, the weighted average overall contains fewer large fluctuations. This combined weighted average of the open magnetic of flux in the northern and southern hemispheres is

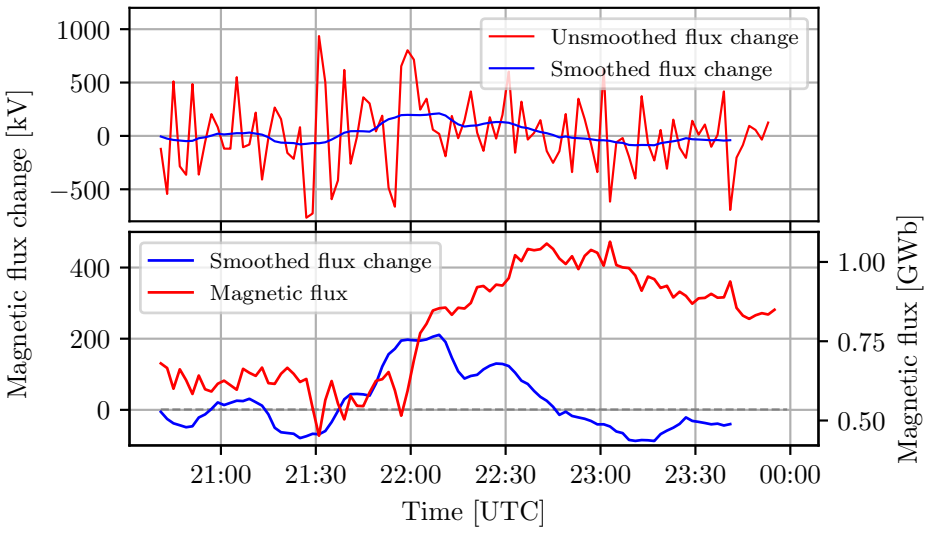

Figure 4.2: The upper plot shows the unsmoothed change in magnetic flux compared to the smoothed flux change obtained by applying first order rolling linear regression to the magnetic flux. The lower plot shows the smoothed flux change with the magnetic flux in the same time window.

what we from now on will be referring to as the open magnetic flux.

From Equation 2.1, we see that the time derivative of the open magnetic flux in the polar cap is equivalent to the nightside reconnection rate subtracted from the dayside reconnection rate. To find this change in open magnetic flux over time, we choose to do a rolling ordinary least squares fit of the flux with each fit on the form

$$y(t) = at + b$$

where y is the open magnetic flux, t is time, a is the slope and b is the intercept. By performing a rolling linear fit, we also smoothen and filter the flux change. This means that for each iteration of the rolling linear fit, we can use the slope a to find the net reconnection rate for the point in time in the middle of the time series used for the linear fit. Because the time between measurements is two minutes, we decide to use fifteen points for each linear fit such that each fit consists of measurements over 30 minutes. Using a larger interval would result in a stronger smoothing of the flux change and could potentially result in loss of important detail and inability to capture substorm fluctuations, while using a smaller interval leads to less noise filtering. *Partamies et al.* [2013] found that the median lengths for the growth and recovery phases of a substorm were 31 minutes. This means that we should refrain from using longer intervals during smoothing, as this could lead to loss of data for the substorm growth phase (when

dayside reconnection is dominating) or the recovery phase (when nightside reconnection is dominating). Figure 4.2 shows a comparison between the smoothed flux change plotted against the unsmoothed flux change, as well as a plot of the magnetic flux and the corresponding smoothed flux change. The unsmoothed flux change was obtained for each time point i as

$$\frac{\Delta F_{PC,\ i}}{\Delta t_i} = \frac{F_{PC,\ i} - F_{PC,\ i-1}}{t_i - t_{i-1}}, \tag{4.1}$$

where $\Delta F_{PC,\ i}/\Delta t_i$ is the flux change, and $F_{PC,\ i}$ and $F_{PC,\ i-1}$ are the polar cap open magnetic flux at time t_i and t_{i-1} respectively. The figure shows that the rolling linear fit leads to significant smoothing of the flux change. However, the smoothed flux change is still able to follow the general shape of the raw flux change. The points when the smoothed flux change is zero coincide with the approximate local maxima and local minima of the magnetic flux. Additionally, the local maxima and local minima of the flux change coincide with periods of large relative increase and decrease respectively in the magnetic flux.

Furthermore, it is clear from Equation 2.1 that a positive change in open magnetic flux in the polar cap indicates that the dayside reconnection rate is larger than the nightside reconnection rate, whereas a negative flux change would indicate a larger nightside reconnection rate than that of the dayside. Because we only have one equation and two unknowns, we assume that a negative flux change means that nightside reconnection is dominating so that

$$\Phi_N = -\frac{dF_{PC}}{dt} \text{ and } \Phi_D = 0 \text{ if } \frac{dF_{PC}}{dt} < 0, \tag{4.2}$$

while a positive flux change means that dayside reconnection is dominating so that we have

$$\Phi_D = \frac{dF_{PC}}{dt} \text{ and } \Phi_N = 0 \text{ if } \frac{dF_{PC}}{dt} > 0. \tag{4.3}$$

This separation means that our dayside rates and nightside rates can never simultaneously be non-zero. Figure 4.3 shows this separation of the magnetic flux change, $\Phi_N - \Phi_D$, into the dayside reconnection rate Φ_D and the nightside reconnection rate Φ_N. We observe that the negative magnetic flux change value is assigned to the nightside rate, whereas the positive flux change value is assigned to the dayside rate.

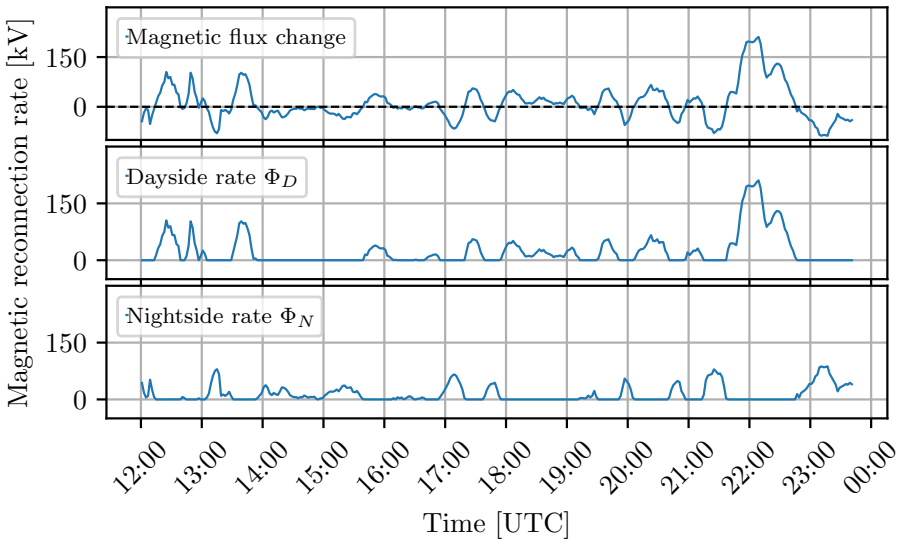

Figure 4.3: The upper plot shows the total magnetic reconnection rate as the sum of the dayside and nightside reconnection rates. The middle and lower plots show the separate dayside and nightside rates respectively.

4.2 Filtering on IMF stability

The overall purpose of this project is to model the dayside and nightside reconnection rates based on certain conditions in the IMF leading to magnetic coupling between the IMF and the Earth's magnetosphere. *Ridley et al.* [1998] estimated in their statistical study on IMF conditions and subsequent ionospheric convection that it takes 8.4($\pm$ 8.2) minutes for the ionosphere to respond to a change in the IMF, as well as 13 minutes on average for the ionosphere to fully reconfigure. Furthermore, they also found from previous studies [*Ridley et al.*, 1998, and references therein] that the time between an IMF change and a resulting reaction in the ionosphere was normally between 3-10 minutes, and between 10-25 minutes for the ionospheric convection to fully reconfigure. Due to this potential delay between the IMF conditions and the subsequent magnetic coupling, as well as the uncertainty from propagating the IMF measurements to the bow shock, we need to establish a stability criterion to ensure that the events we consider originated from sufficiently stable IMF conditions.

To ensure IMF stability, we use the stability criterion defined by *Haaland et al.* [2007], which is based on demanding that the IMF Y and Z components propagated to the bow shock within a time interval are close to parallel. For a chosen point in time, we consider the IMF measured at that point, as well as IMF measurements from a time interval directly preceding and following

the chosen point. For the combined time interval, we calculate the mean of the normalised IMF By, Bz vectors within the interval, which we refer to as the bias vector, and use its length as a measure of the spread of the direction of the individual IMF vectors within the time interval. If all the vectors were perfectly parallel, the bias vector length would be of unit length, while a bigger spread in IMF directions would lead to a shorter bias vector length. The steps of the method are as follows:

1. Choose one measurement of the IMF By, Bz components at a certain time point.
2. Consider a time interval spanning from a time point before and after the chosen point.
3. Normalise each IMF vector in the time interval
4. Calculate the bias vector as the mean of the normalised vectors
5. If the length of the bias vector is below a given threshold, the initially chosen IMF is considered unstable and excluded from the study.

Haaland et al. [2007] used a total time interval of 30 minutes, with the interval starting 20 minutes before the chosen IMF measurement and ending 10 minutes after, while the threshold for the bias vector length was chosen as 0.96 as a compromise between sufficient filtering and leaving enough data for statistical stability. This interval was chosen to account for bow shock propagation uncertainty [*King and Papitashvili*, 2005], as well as the time needed for the ionosphere to respond to a change in the IMF. Using the same values, we are left with around 616k stable IMF values out of the original 1.8 million measurements.

4.3 Sectioning the rates

We divide the remaining IMF Bz measurements based on their values into ten bins. Each bin consists of the same amount of IMF measurements so that each interval contains around 61.6k IMF Bz values. For each IMF measurement within these IMF Bz intervals, we consider the dayside and nightside reconnection rates every two minutes from the time the given IMF measurement was taken to 90 minutes after. This means that the reconnection rates within one IMF Bz interval are divided into 92 sets of rates, with one set consisting of either dayside or nightside reconnection rates given a time (0, 2, 4, ..., 90 minutes) after the initial IMF Bz value, for a total of 46 sets of dayside rates and 46 sets of nightside rates respectively. This structure is illustrated in Figure 4.4 for one IMF interval. We have ten such intervals, meaning we have a total of 920 sets of reconnection rates, with each set containing up to 61.6k samples each.

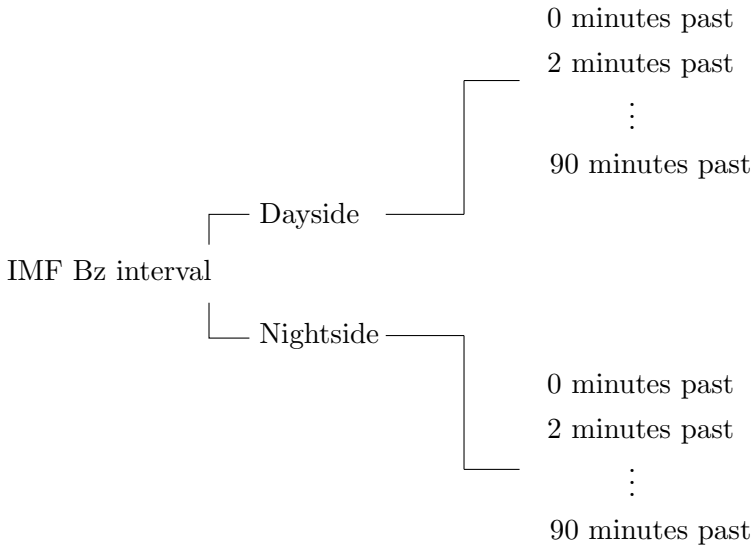

Figure 4.4: Illustration of the dataset structure of reconnection rates for one IMF Bz interval. For each interval, there is a separation between the dayside and the nightside reconnection rate for the reconnection rates 0, 2, . . . , 90 minutes after the initial IMF value.

4.4 Modelling distributions

We want to be able to sample new reconnection rate values based on the values of our distributions of reconnection rates. To achieve this, we first need to find distributions that closely resemble those of our rates. For each IMF Bz interval we have 92 sets, as shown in Figure 4.4, which all need to be described by a suitable distribution and corresponding parameters. We have ten IMF intervals we need to fit separate distributions for, totalling up to 920 distributions.

When separating the dayside and nightside reconnection rates as described in Equation 4.2 and 4.3, we imposed that neither could be simultaneously non-zero. This leads to the sets containing an unnaturally high proportion of zeros that would be difficult to replicate using a theoretical distribution function. To circumvent this, we exclude the zeros when fitting a distribution to our set and instead choose to add them back when generating the full time series of rates. The way in which we reintroduce the zero values will be elaborated on in section 4.5. The distribution of one set of reconnection rates is shown in Figure 4.5, as well as the distribution of the same set with the zero values excluded. We see that the occurrence of zeros is artificially high and occurs far more frequently than any other value. After removing the zeros, we see that the distribution density is higher for lower reconnection rate values and decreases sharply as reconnection rate

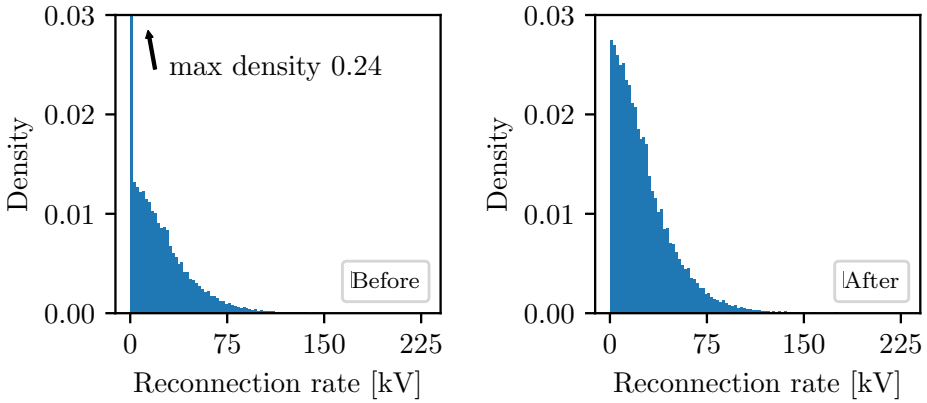

Figure 4.5: The left plot shows the distribution density of one of the sets of reconnection rates. The right plot shows the distribution of the same set, but with the zero values removed.

increases.

Following some experimentation, we decide on representing the distributions of the reconnection rates as gamma distributions. One parametrisation of the gamma probability density function is given by

$$f(x;k,\theta) = \frac{x^{k-1}}{\theta^k \Gamma(k)} e^{-x/\theta} \ , \tag{4.4}$$

where x is the reconnection rate, k is the shape, θ is the scale and $\Gamma(k)$ is the gamma function, with $x,\ k,\ \theta > 0$. While the shape parameter k determines the skewness of the distribution, the scale parameter θ determines the scale of the distribution. By changing the shape parameter, we can account for different levels of skewness in the distributions, while the scale parameter can adjust the size of the reconnection rate values. This means that the parameters can be fitted according to each set of reconnection rates.

We use the Metropolis-Hastings (MH) algorithm in order to find gamma distribution parameters that most closely resemble each of our sets of reconnection rates. The algorithm goes as follows for N iterations [e.g. *Ruanaidh and Fitzgerald*, 1996]:

1. Start with an initial guess of parameters y_i.
2. For each iteration i:
   - Sample new candidate set of parameters y_i' from a symmetric proposal distribution $Q(y_i'|y_i)$.
   - Calculate the acceptance ratio

$$\alpha = \frac{f(y_i')P(y_i')}{f(y_i)P(y_i)}, \tag{4.5}$$

where $P(y_i)$, $P(y_i')$ is the prior probability and $f(y_i),\ f(y_i')$ is the probability density function that is proportional to the target distribution.

- Generate a random number $r \in [0,\ 1]$.
  - If $r \leq \alpha$: Accept the new set of parameters, $y_{i+1} = y_i'$
  - If $r > \alpha$: Reject the new set of parameters, $y_{i+1} = y_i$

We execute the MH algorithm using the following configuration for all the sets of reconnection rates:

- Initial parameter values $k_i = 1.0,\ \theta_i = 30.0$.
- $N = 80000$ number of iterations.
- Gaussian proposal distributions Q_k and Q_θ so that $k_i'|k_i \sim \mathcal{N}(k_i,\ 0.01^2)$ and $\theta_i'|\theta_i \sim \mathcal{N}(\theta_i,\ 1.3^2)$.
- Gamma probability density function, see Equation 4.4.
- Prior $k > 0$, $\theta > 0$.

The code used to run MH was based on an article from *Moukarzel* [2018] under the permissive MIT license.

The prior is chosen as such to enforce the range of the gamma distribution $k,\ \theta > 0$. The variances of the Gaussian proposal distributions, as well as the number of iterations, were chosen after some experimentation to ensure that approximately 10-20% of the candidate parameter sets were accepted. By choosing a Gaussian distribution as the proposal distribution, the generated sequences will be a random walk. To find the final shape and scale values, we define them as the mean of the last half of the accepted values, while the error range is defined by the 5th and 95th percentile values. Figure 4.6 shows the first 150 accepted shape and scale parameter values for one set of reconnection rates. The figure also shows the final scale and shape values, along with their corresponding error range. Both parameters in this case quickly start converging towards the final values and are mostly able to stay within the error lines after 50 iterations. Figure 4.7 shows all accepted shape values for the same set of reconnection rates with the same red dashed lines as before. The figure also shows the distribution of the second half of all the accepted shape values. Although the error range is based on the second half of all the accepted values, the scale converges quickly enough for most of the values in the first half of accepted iterations to fit within this range. Because we used a Gaussian proposal distribution, the probability density for the accepted shape values appears to be symmetrical around the mean. The most typical shape values are contained within the error range defined by the 5th and 95th percentiles.

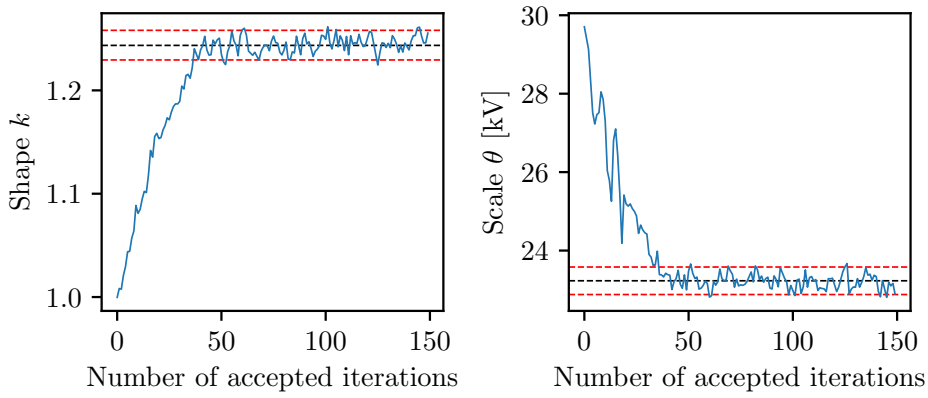

Figure 4.6: The plots show the first 150 accepted gamma distribution parameter values obtained through the Metropolis-Hastings algorithm for one set of reconnection rates. The left plot shows shape values while the right plot shows the scale values. The red dashed lines show the error ranges as the 5th and 95th percentile values of the second half of all accepted values. The black lines show the mean of the second half of all accepted values.

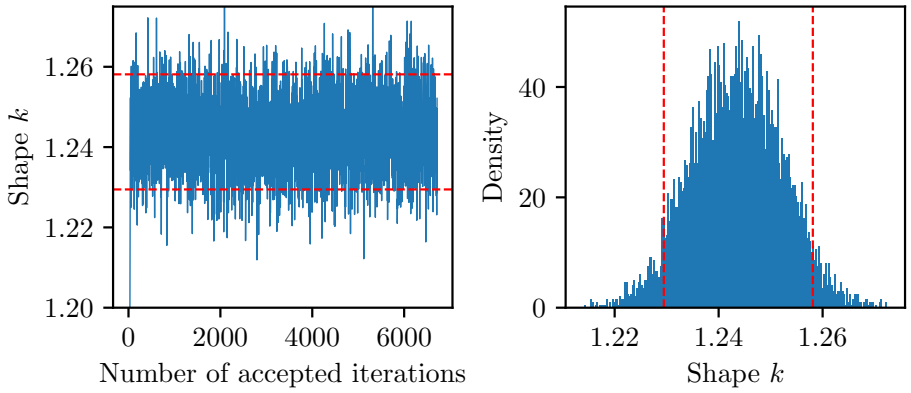

Figure 4.7: The left plot shows the accepted shape values for one set of reconnection rates found via the Metropolis-Hastings algorithm with the red dashed lines representing the error range as the 5th and 95th percentile values of the second half of the accepted values. The right plot shows the distribution of the second half of the accepted shape values with the dashed lines still representing the error values.

4.5 Generating synthetic reconnection rates

Using the MH algorithm for each reconnection rate set as described in section 4.4, we obtain 920 pairs of shape and scale gamma distribution parameters. By sampling from these gamma distributions, we can generate new reconnection rates based on a given initial IMF Bz value for the subsequent 90 minutes.

The algorithm samples from gamma distributions using the mean shape and scale values as obtained in section 4.4 to generate N time series of dayside and nightside reconnection rates. The steps are:

1. Give an initial IMF Bz value
2. For every iteration $n = 1, 2, \ldots, N$:
   (a) For every time point t:
      i. Calculate a ratio p of the number of non-zero data points m over the number of total data points in all registered nightside reconnection rates n for that IMF interval and time point,

$$p_t = \frac{m_t}{n_t} \tag{4.6}$$

      ii. Generate random number $a \in [0, 1]$.
         - If $p_t \leq a$: Generate a value for the nightside rate value by sampling a value from the gamma distribution given by the corresponding shape and scale values found via MH. Set dayside reconnection rate value to zero.
         - If $p_t > a$: Generate a value for the dayside rate value by sampling a value from the gamma distribution given by the corresponding shape and scale values found via MH. Set nightside reconnection rate value to zero.

Additionally, you can choose to sample reconnection rates from the gamma distributions given by shape and scale values randomly sampled from a uniform distribution within their respective confidence intervals. To ensure some level of statistical stability, we choose to sample N sets of reconnection rates for M number of sets of gamma parameters. This means that every set of shape and scale parameters generate more than only one set of time series. The algorithm then becomes:

1. Give an initial IMF Bz value
2. For every time point t:
   (a) Calculate the ratio p_t as in Equation 4.6
   (b) For every iteration $m = 1, 2, \ldots, M$:

i. Sample nightside shape k'_N and scale θ'_N values from the uniform distributions spanned by their respective confidence intervals, $k'_N \sim \mathcal{U}(k_N^{\min},\ k_N^{\max})$ and $\theta'_N \sim \mathcal{U}(\theta_N^{\min}, \theta_N^{\max})$.

ii. Sample dayside shape k'_D and scale θ'_D values from the uniform distributions spanned by their respective confidence intervals, $k'_D \sim \mathcal{U}(k_D^{\min},\ k_D^{\max})$ and $\theta'_D \sim \mathcal{U}(\theta_D^{\min}, \theta_D^{\max})$.

iii. For every iteration $n = 1, 2, \ldots, N$:

- Generate a random number $a \in [0,\ 1]$.
- If $p_t \leq a$: Generate a value for the nightside rate value by sampling from the gamma distribution given by the the shape k'_N and scale θ'_N Set dayside reconnection rate value to zero.
- If $p_t > a$: Generate a value for the nightside rate value by sampling from the gamma distribution given by the the shape k'_D and scale θ'_D Set nightside reconnection rate value to zero.

By using Equation 4.6 and a randomly generated number $a \in [0, 1]$, we are able to reintroduce the zero values that we excluded during the MH algorithm. For a high number of generated time series, the proportions of zeros in the generated reconnection rates should be similar to those of the actual reconnection rates.

Chapter 5

Results

In this chapter we present the results from the distribution parameter fitting using the MH algorithm as explained in section 4.4, as well as the synthetic reconnection rates generated using these parameters according to the method described in section 4.5. The parameters were modelled to fit distributions of reconnection rates that had been filtered and divided into ten bins based on their initial IMF Bz value.

After filtering the IMF measurements on stability, we were left with approximately 616k measurements, which we split into ten equally size bins based on their values. These interval values are found in Table 5.1. We see that there appears to be some degree of symmetry between the positive and negative interval values. For every positive interval range, there is an approximately equal negative interval. These pairs are $[-39.00, -4.03)$ nT and $[4.03, 37.70)$ nT, $[-4.03, -2.48)$ nT and $[2.50, 4.03)$ nT, $[1.47, 2.50)$ nT and $[-2.48, -1.51)$ nT, $[-1.51, -0.73)$ nT and $[0.69, 1.47)$ nT, and $[-0.73, -0.02)$ nT and $[-0.02, 0.69)$ nT. By pairing these

Table 5.1: Table of the IMF Bz intervals found after filtering the IMF on stability and splitting the remaining measurements into ten groups. The intervals were then divided into three different strength classes.

IMF Bz interval [nT]	**Number of values**	**Strength classification**
$[-39.00, -4.03)$	61612	Strong
$[-4.03, -2.48)$	61612	Moderate
$[-2.48, -1.51)$	61612	Moderate
$[-1.51, -0.73)$	61612	Weak
$[-0.73, -0.02)$	61611	Weak
$[-0.02, 0.69)$	61611	Weak
$[0.69, 1.47)$	61611	Weak
$[1.47, 2.50)$	61611	Moderate
$[2.50, 4.03)$	61611	Moderate
$[4.03, 37.70)$	61611	Strong

intervals together, we can directly compare their gamma parameters and reconnection rates. Furthermore, we have chosen to categorise the intervals into strong, moderate and weak based on their reconnection rate values and gamma parameters. These results will be discussed later in section 5.1, section 5.2 and section 5.3.

Figure 5.1 shows the distributions of the dayside and nightside reconnection rates at 0, 30, 60 and 90 minutes past given initial IMF Bz values within the intervals $[-39.00,\ -4.03)$ nT,$[-0.73,\ -0.02)$ nT and $[4.03,\ 37.70)$ nT. The plot also shows the gamma distribution fit for each set found using MH. For the strongly negative interval $[-39.00,\ -4.03)$ nT, the dayside reconnection rate values are more spread at 0 minutes past the initial IMF Bz value and gradually become smaller over time. The nightside reconnection rate shows the opposite pattern, initially showing a higher peak at lower values and gradually flattening. Initially when we have a strongly negative IMF Bz value, we will have higher values of dayside reconnection rate, but as time progresses the nightside reconnection rates will become higher while the dayside reconnection rates will diminish. For the weakly negative interval $[-0.73,\ -0.02)$ nT there is a less clear distinction between the dayside and nightside rates over 90 minutes. Both the dayside and nightside distributions have a relatively sharp peak, meaning the reconnection rates are generally low within these initial IMF Bz values. For the strongly positive interval $[4.03,\ 37.70)$ nT there is a similar pattern to the one for the interval $[-39.00,\ -4.03)$ nT, but reversed. The dayside rate distributions have a sharper peak initially and gradually spread out, while the nightside rate distributions gradually develop a sharper peak. However, the difference in width and spread between the dayside and nightside rates within this interval is smaller than for the corresponding negative interval $[-39.00,\ -4.03)$ nT. Additionally, the dayside and nightside reconnection rate distributions are overall more spread and wider with a lower peak than their counterparts in the negative IMF interval. The change in distributions over time in the positive IMF Bz interval are less extreme than in the negative interval.

The fitted gamma distributions are able to follow the general shape of the actual distributions closely. The tails of the fitted distributions replicate the tails of the actual distributions well. However, the fitted distributions have consistently higher peaks the than observed distributions. This is particularly evident for flatter distributions with higher shape parameter values.

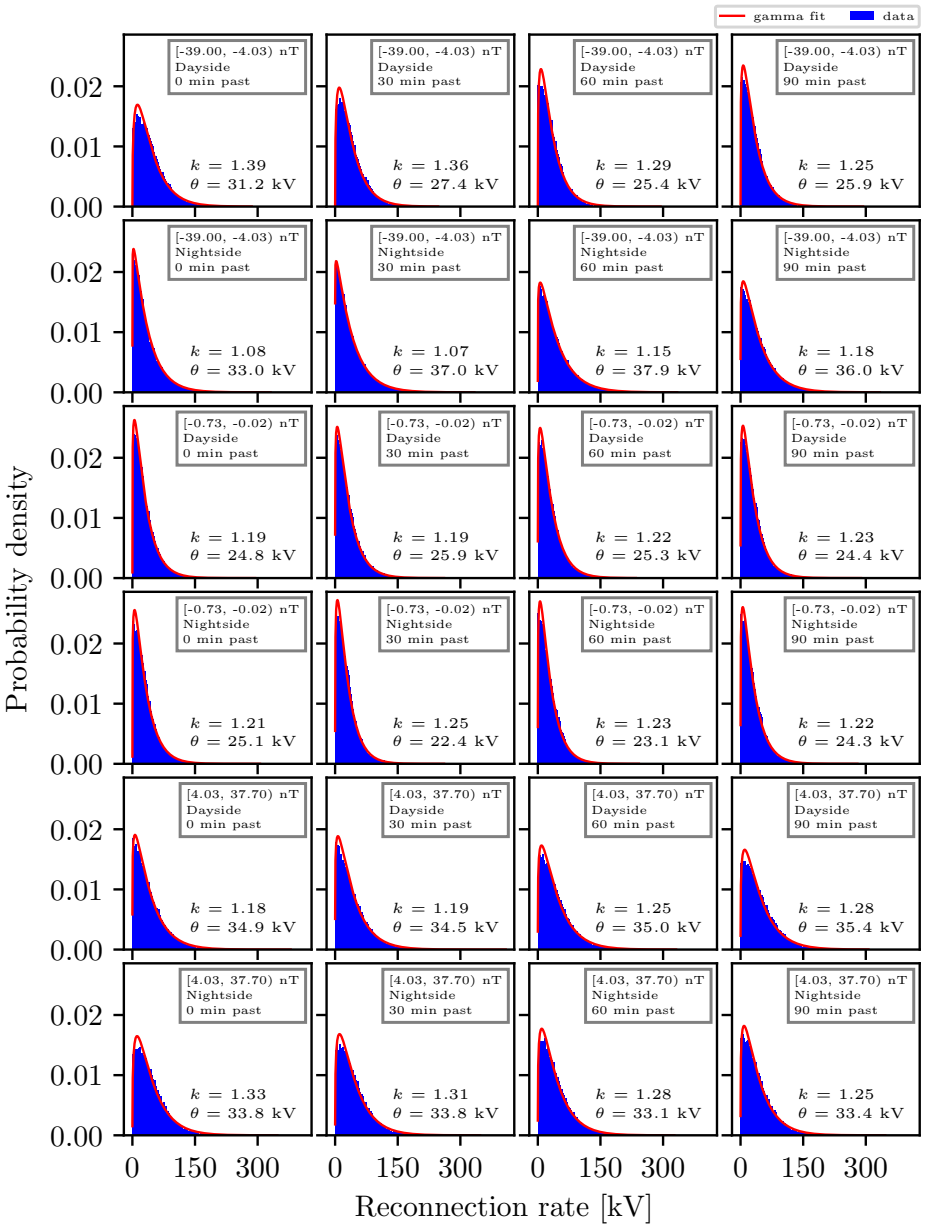

Figure 5.1: The distribution densities of selected sets of reconnection rates plotted along with their gamma distribution fits with shape and scale parameters k, θ. The two uppermost rows show the distribution of the rates given initial IMF Bz values in the interval $[-39.00,\ -4.03)$ nT at 0, 30, 60 and 90 minutes past the initial IMF value. The two middle rows show the corresponding sets for the interval $[-0.73,\ -0.02)$ nT, and the two last rows for the interval $[4.03,\ 37.7)$ nT.

5.1 Strong IMF

Figure 5.2 shows the values for the gamma distribution parameters shape and scale for the strong IMF Bz intervals [4.03, 37.70) nT and [−39.00, −4.03) nT over time found using MH. For the shape values in the IMF Bz interval [4.03, 37.70) nT we see that the nightside values are initially larger than the dayside values.

The nightside shape decreases over the 90 minute time window as the dayside shape increases and becomes smaller than the dayside shape after around 60-70 minutes have passed. The pattern for the shape values in the IMF Bz interval [−39.00, −4.03) nT show a similar reversed pattern. The dayside shape values are initially larger than the nightside shape values, but decrease over time while the nightside shape values increase. However, the dayside and nightside shape values do not cross within the 90 minute time window. There is also a significantly larger difference between the dayside and nightside values for the [−39.00, −4.03) nT interval than for [4.03, 37.70) nT. The difference between the dayside and nightside scale values in the [4.03, 37.70) nT interval is initially very small, but increases slightly after 40 minutes. The dayside scale values are larger than the nightside values throughout the time interval, with some overlap within their confidence intervals until 40 minutes have passed since the initial IMF Bz value. Within the [−39.00, −4.03) nT interval there is a significantly larger difference between the dayside and nightside scale values. The nightside scale is consistently higher than the dayside scale throughout the entire time window, with the difference between the two being smallest initially. The difference gradually increases over time and decreases slightly after 60 minutes.

Figure 5.3 shows the mean values of synthetic 50 000 reconnection rates generated using gamma distributions with the shape and scale parameter values shown in Figure 5.2 for the IMF Bz intervals [4.03, 37.70) nT and [−39.00, −4.03) nT. The coloured areas show the mean values of reconnection rates generated using shape and scale samples randomly sampled from within their respective confidence intervals. For the IMF Bz interval [4.03, 37.70) nT the mean generated nightside reconnection rates are larger than the mean of the generated nightside rates until around 55 minutes when the mean dayside rates become larger. The mean nightside rate declines slowly the first 25 minutes before rapidly declining throughout the rest of the time window. The mean dayside rate seems to mirror the nightside pattern. For the IMF Bz interval [−39.00, −4.03) nT the mean generated dayside rates are initially larger than the mean generated nightside rates. The mean dayside rates decrease as the mean nightside rates increase and meet after around 40 minutes. The mean nightside rates stay larger than the mean dayside rates the remaining time window. Comparing the synthetic dayside and nightside reconnection rates within the two IMF Bz intervals

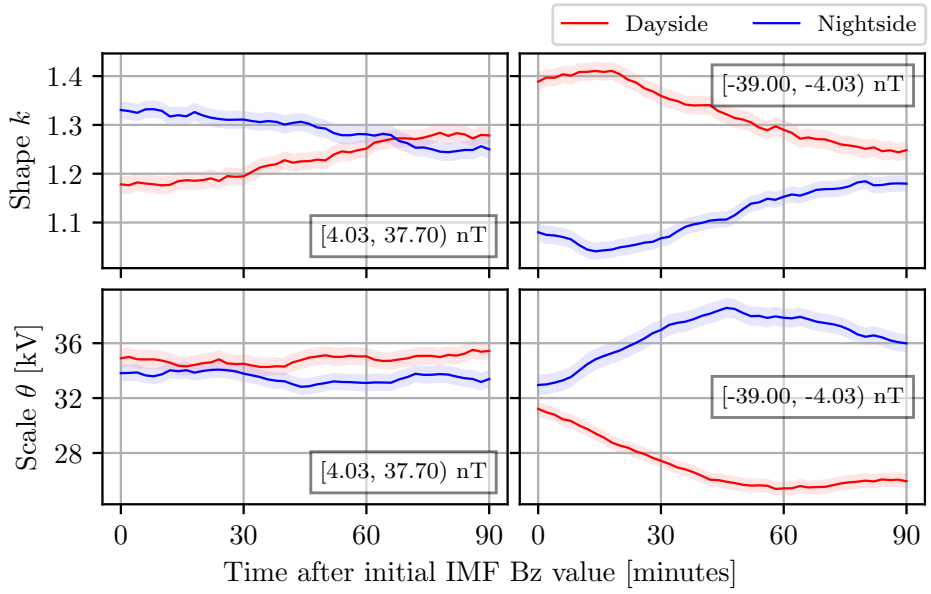

Figure 5.2: Shape and scale gamma distribution parameters over time found using the Metropolis-Hastings algorithm. The left shows the parameters for the IMF Bz interval [4.03, 37.70) nT. The right shows the parameters for the interval [−39.00, −4.03) nT.

[4.03, 37.70) nT and [−39.00, −4.03) nT, we see that the maximum and minimum rates for the negative interval [−39.00, −4.03) nT are much higher and lower respectively. The mean reconnection rates in the negative interval fall between approximately 12.5 kV and 27.5 kV, while the mean rates in the positive interval fall between 17.5 kV and 26 kV. The maximum difference between the mean dayside and nightside rates are approximately 15 kV, compared to the 8 kV difference in the positive IMF Bz interval. This corresponds well with the difference in the shape and scale values of their respective gamma distributions.

When comparing the mean generated rates with the actual rates, we see that our algorithm is able to generate mean rates that approximately follow the shape and values of the mean of the actual rates for both these IMF Bz intervals. The points at which the rates cross occur at the same time for both the actual rates and the synthetic rates.

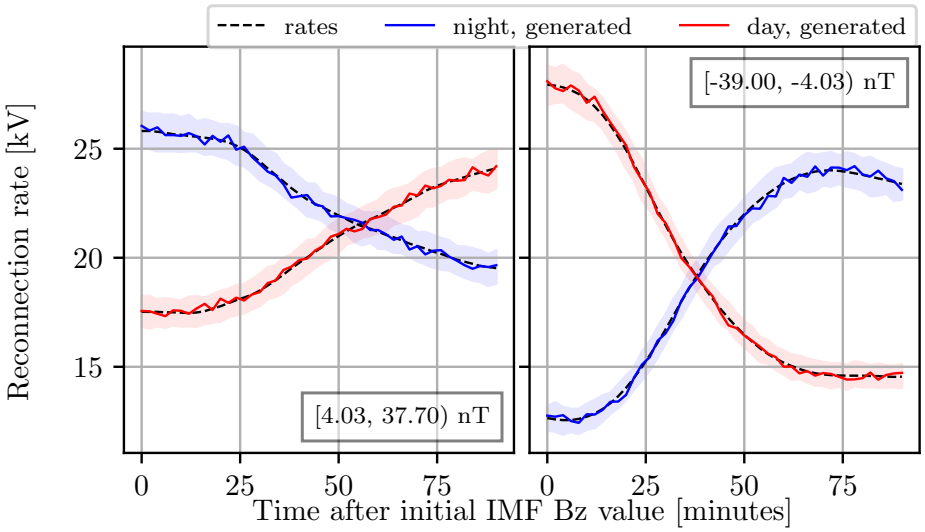

Figure 5.3: The mean values of 50 000 generated dayside and nightside reconnection rates using initial IMF Bz values within the intervals [4.03, 37.70) nT and [−39.00, −4.03) nT. The dashed lines show the mean values of the actual reconnection rates within the same interval.

5.2 Moderate IMF

Figure 5.4 shows the values for the gamma distribution parameters shape and scale for the moderate IMF Bz intervals [2.50, 4.03) nT and $[-4.03, -2.48)$ nT over time found using MH, while Figure 5.5 shows the gamma distribution parameters for the IMF Bz intervals [1.47, 2.50) nT and $[-2.48, -1.51)$ nT. For the positive intervals [2.50, 4.03) nT and [1.47, 2.50) nT, both the shape and scale values show similar patterns. In the shape plots, we see that the the nightside shape values are initially larger than the dayside values. The nightside shape values decrease slowly the entire time window while the dayside values increase. The nightside shape decreases slowly the first quarter before declining more rapidly, with the dayside shape mirroring this pattern and increasing faster after the first quarter. They eventually cross after roughly one hour, after which the dayside shape values become larger. The shape plots for both the negative IMF Bz intervals $[-4.03, -2.48)$ nT and $[-2.48, -1.51)$ nT show that the dayside shape values are initially larger than those of the nightside, but the nightside shape values eventually become larger towards the end. For the stronger interval $[-4.03, -2.48)$ nT, the dayside shape decreases steadily throughout the entire time window, while the nightside shape increases slowly before rapidly increasing and eventually stabilising at the end. For the interval $[-2.48, -1.51)$ nT, the dayside values are initially stable the

first half before declining the rest of the time window, whereas the nightside values increase slowly the entire time.

The scale plots for both positive IMF Bz intervals [2.50, 4.03) nT and [1.47, 2.50) nT show that the dayside and nightside scale values remain relatively stable throughout the full time window. The dayside scales are initially larger than those of the nightside, but slowly decrease in the second half. The nightside scales slowly increase as the dayside scales decrease, eventually meeting the dayside scales with both overlapping at the end of the time window. For the negative IMF Bz intervals $[-4.03, -2.48)$ nT and $[-2.48, -1.51)$ nT, there is initially an overlap in dayside and nightside scale values. The dayside and nightside scales eventually diverge and end with the nightside scale being larger than the dayside scale. It takes approximately 45 minutes for the dayside and nightside to fully diverge in the $[-2.48, -1.51)$ nT interval, compared to approximately 15 minutes in the $[-4.03, -2.48)$ nT interval. When comparing the negative intervals $[-4.03, -2.48)$ nT and $[-2.48, -1.51)$ nT to their positive counterparts, the positive intervals [2.50, 4.03) nT and [1.47, 2.50) nT have significantly higher scale parameter values.

Figure 5.6 shows the mean values of synthetic 50 000 reconnection rates generated using gamma distributions with the shape and scale parameter values shown in Figure 5.4 for the IMF Bz intervals [2.50, 4.03) nT and $[-4.03, -2.48)$ nT, while Figure 5.7 shows those of the intervals [1.47, 2.50) nT and $[-2.48, -1.51)$ nT using the gamma parameters shown in Figure 5.8. For initial IMF Bz values within the positive intervals [2.50, 4.03) nT and [1.47, 2.50) nT, the mean nightside reconnection rates are initially higher than the mean dayside rates and decrease throughout the full time window. The mean dayside reconnection rates mirror the nightside and increase as the mean nightside rates decrease, eventually crossing the mean nightside rate and becoming bigger. The dayside and nightside mean reconnection rates intersect after around 55-60 minutes. For initial IMF Bz values within the negative intervals $[-4.03, -2.48)$ nT and $[-2.48, -1.51)$ nT, the dayside mean reconnection rates are initially larger than those of the nightside. The mean dayside reconnections seem to slightly increase in the first 20-25 minutes before decreasing the rest of the time window. The mean nightside reconnection rates mirror the dayside and decrease slightly in the beginning before increasing the rest of the time window. The mean rates cross after 40 minutes for the $[-4.03, -2.48)$ nT interval and after around 60 minutes for the $[-2.48, -1.51)$ nT interval. As with the scale values shown in Figure 5.4 and Figure 5.5, there is a significant discrepancy between the reconnection rate values with positive initial IMF Bz values compared to their negative counterparts. The mean reconnection rate values are within the range 17.5 kV to 23 kV for the positive [2.50, 4.03) nT interval compared to range 10 kV to 20 kV for the negative $[-4.03, -2.48)$ nT interval, and the range 16.5 kV to 22 kV for the positive interval [1.47, 2.50) nT compared to the range

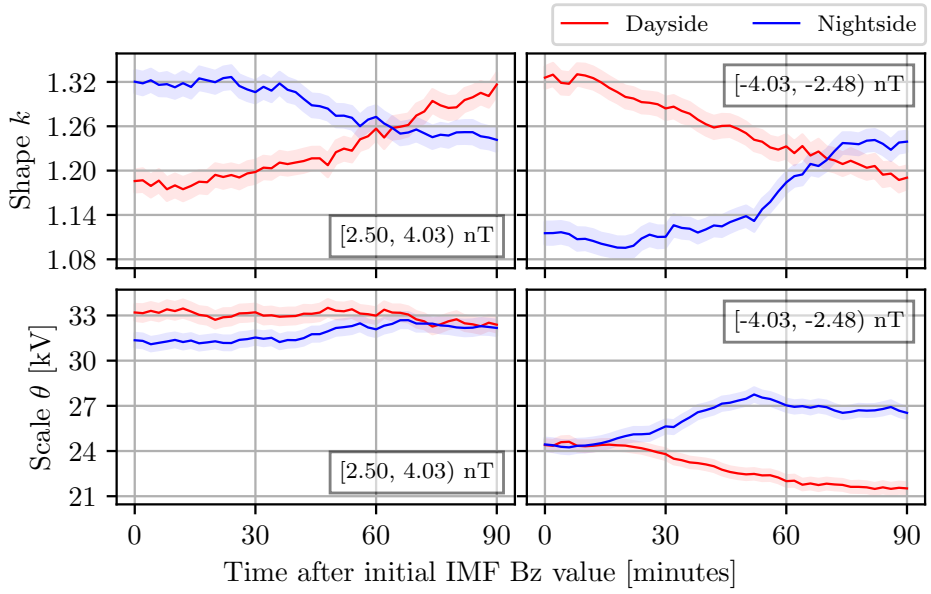

Figure 5.4: Shape and scale gamma distribution parameters over time found using the Metropolis-Hastings algorithm. The left shows the parameters for the IMF Bz interval $[2.50,\ 4.03)$ nT. The right shows the parameters for the interval $[-4.03, -2.48)$ nT.

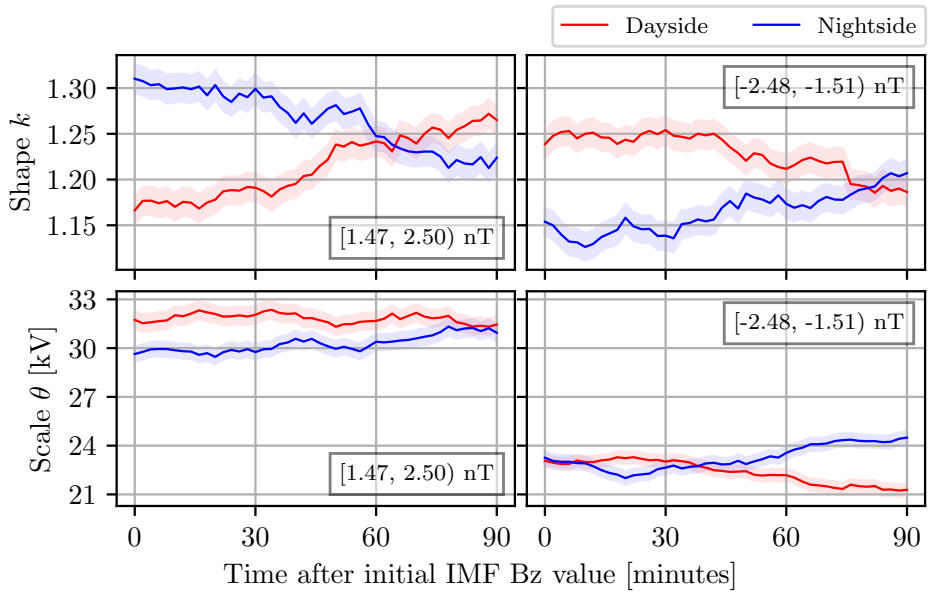

Figure 5.5: Shape and scale gamma distribution parameters over time found using the Metropolis-Hastings algorithm. The left shows the parameters for the IMF Bz interval $[1.47,\ 2.50)$ nT. The right shows the parameters for the interval $[-2.48, -1.51)$ nT.

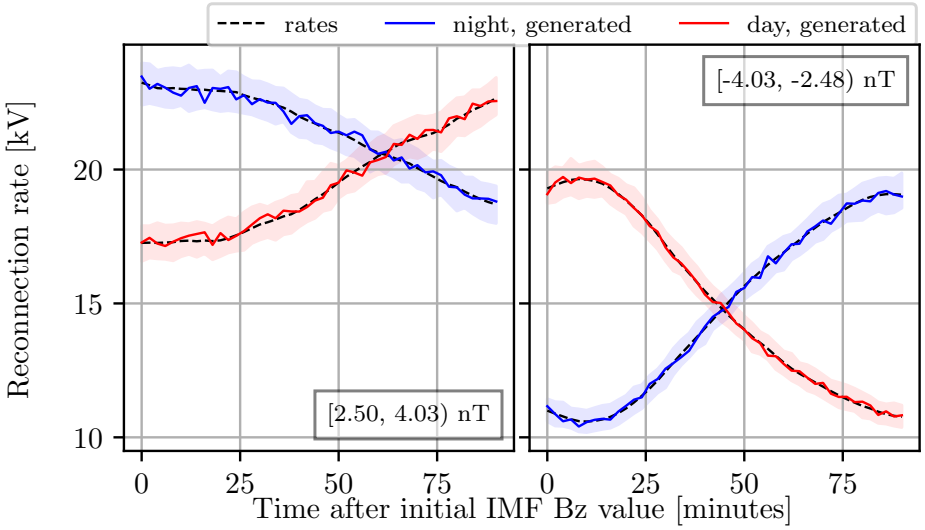

Figure 5.6: The mean values of 50 000 generated dayside and nightside reconnection rates using initial IMF Bz values within the intervals $[2.50,\ 4.03)$ nT and $[-4.03, -2.48)$ nT. The dashed lines show the mean values of the actual reconnection rates within the same interval.

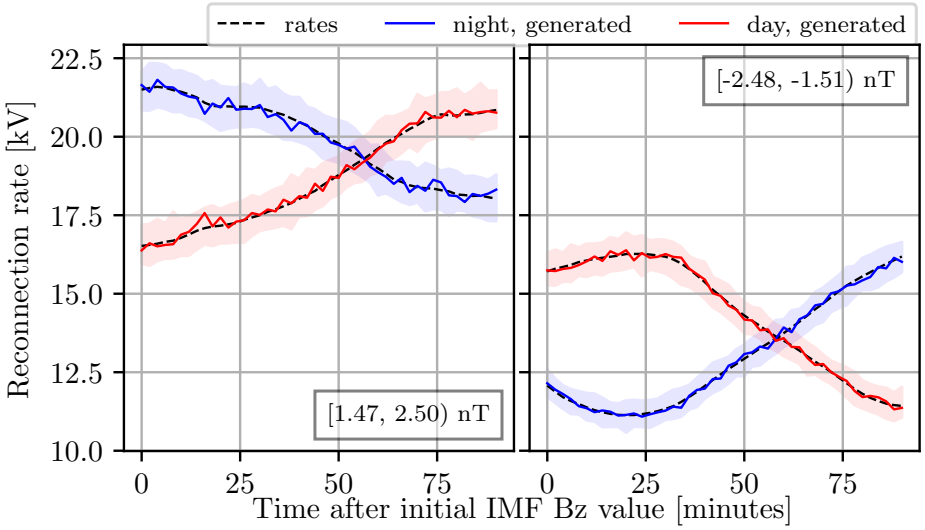

Figure 5.7: The mean values of 50 000 generated dayside and nightside reconnection rates using initial IMF Bz values within the intervals $[1.47,\ 2.50)$ nT and $[-2.48, -1.51)$ nT. The dashed lines show the mean values of the actual reconnection rates within the same interval.

11 kV and 16.5 kV for the negative $[-2.48, -1.51)$ nT interval.

When comparing the mean synthetic reconnection rates to the mean of the actual reconnection rates, we see that the mean synthetic rates are able to follow the pattern of the mean of the actual rates closely and the points at which the dayside and nightside mean rates intersect are the same. The gamma distributions for the negative IMF Bz values are able to generate mean synthetic rates that more accurately represent the actual mean rates. However, the means of the actual reconnection rates from all four IMF Bz intervals are within the error ranges of the mean synthetic rates.

5.3 Weak IMF

Figure 5.8 shows the values for the gamma distribution parameters shape and scale for the weak IMF Bz intervals $[0.69,\ 1.47)$ nT and $[-1.51, -0.73)$ nT over time found using MH, while Figure 5.9 shows the gamma distribution parameters for the IMF Bz intervals $[-0.02,\ 0.69)$ nT and $[-0.73,\ -0.02)$ nT. We observe that the shape and scale plots for the positive interval $[0.69,\ 1.47)$ nT and mostly positive interval $[-0.02,\ 0.69)$ nT show similar patterns. For both intervals, the nightside shape values are initially higher than the dayside values. The nightside shape values increase at the beginning of the time window, but gradually decrease the rest of the time window. The dayside shape values increase throughout most of the time window and eventually overlaps with the nightside values at the end. The shape plots for the negative IMF Bz intervals $[-1.51,\ -0.73)$ nT and $[-0.73,\ -0.02)$ nT are however quite different. The dayside and nightside shape values for the $[-1.51,\ -0.73)$ nT overlap through most of the time window, with the dayside shape value being slightly larger in the beginning. There does not appear to be any discernible pattern in the shape values, nor do the values change much overall. The shape plot for the interval $[-0.73,\ -0.02)$ nT shows that the nightside shape values are initially higher than the dayside values. The nightside shape values increase slightly before decreasing towards the end, whereas the dayside shape values appear to increase overall and eventually overlap with and surpass the nightside values towards the end.

The scale plots for all four IMF Bz intervals show that the dayside scale values are higher than the nightside scale values for most of the time window. For the positive interval $[0.69,\ 1.47)$ nT and mostly positive interval $[-0.02,\ 0.69)$ nT, the dayside scale values are relatively stable and stay higher than the nightside values during the full time period. For the $[0.69,\ 1.47)$ nT interval the dayside scale decreases slightly towards the end, while the dayside scale for the $[-0.02,\ 0.69)$ nT interval increases slightly towards the end before decreasing again. The nightside scale values for both positive intervals decrease slightly towards the middle of the time period,

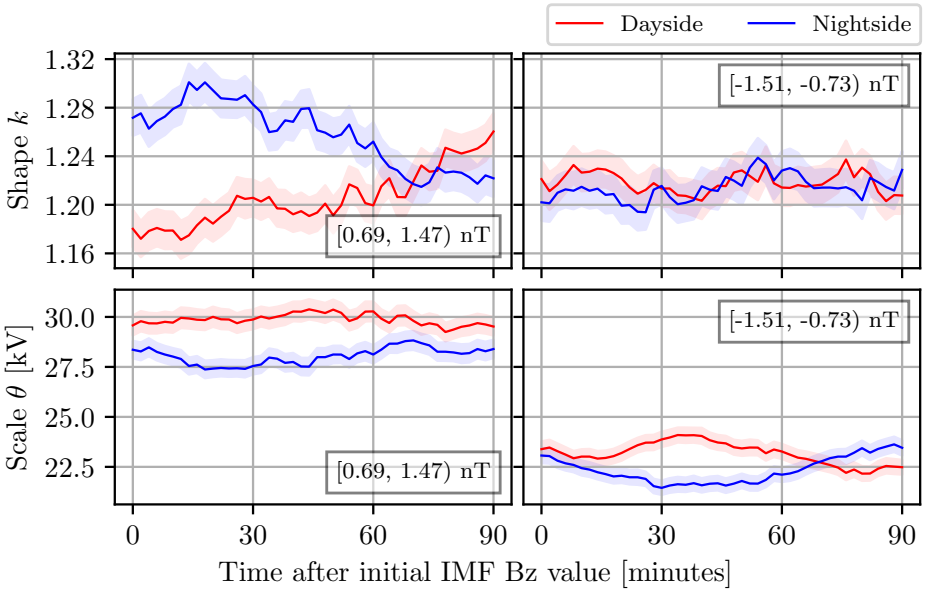

Figure 5.8: Shape and scale gamma distribution parameters over time found using the Metropolis-Hastings algorithm. The left shows the parameters for the IMF Bz interval $[0.69,\ 1.47)$ nT. The right shows the parameters for the interval $[-1.51, -0.73)$ nT.

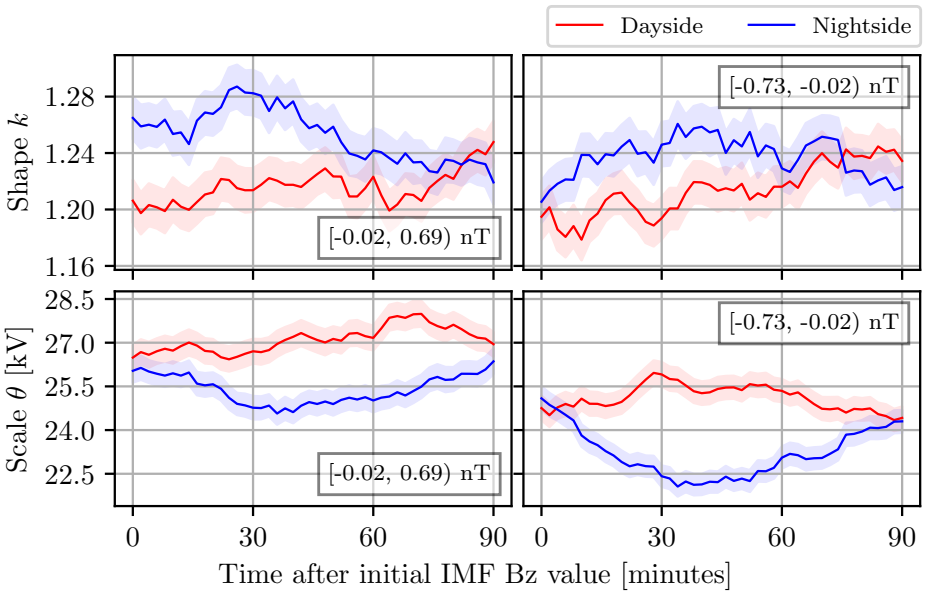

Figure 5.9: Shape and scale gamma distribution parameters over time found using the Metropolis-Hastings algorithm. The left shows the parameters for the IMF Bz interval $[-0.02,\ 0.69)$ nT. The right shows the parameters for the interval $[-0.73, -0.02)$ nT.

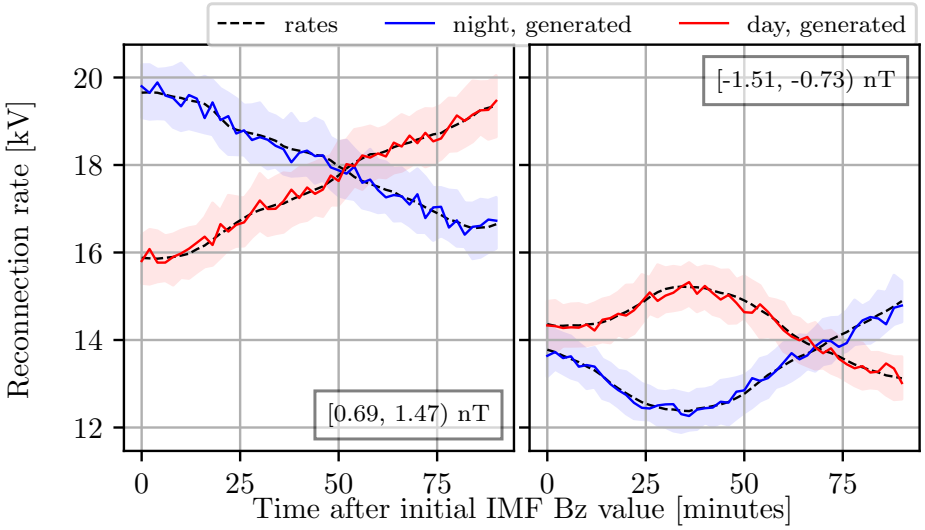

Figure 5.10: The mean values of 50 000 generated dayside and nightside reconnection rates using initial IMF Bz values within the intervals [0.69, 1.47) nT and $[-1.51, -0.73)$ nT. The dashed lines show the mean values of the actual reconnection rates within the same interval.

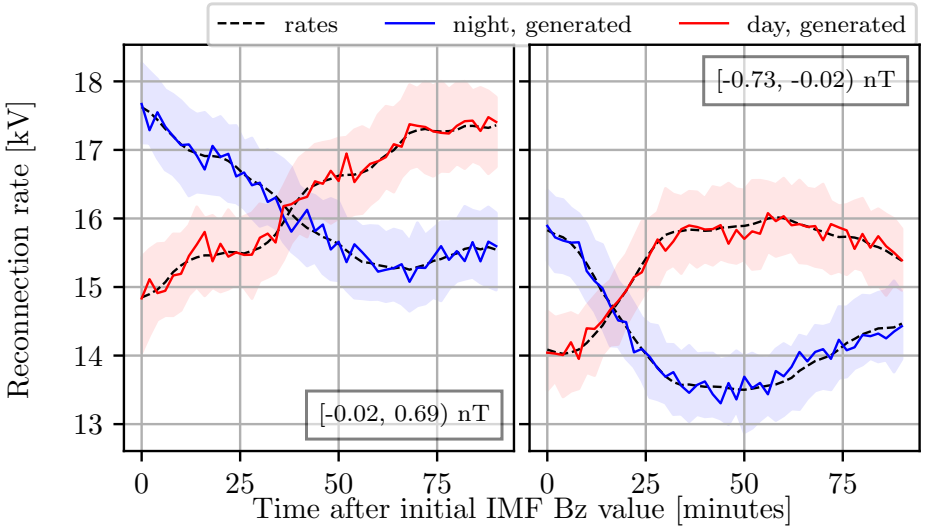

Figure 5.11: The mean values of 50 000 generated dayside and nightside reconnection rates using initial IMF Bz values within the intervals $[-0.02, 0.69)$ nT and $[-0.73, -0.02)$ nT. The dashed lines show the mean values of the actual reconnection rates within the same interval.

but increase again towards the end. In scale plots for both the negative IMF Bz intervals $[-0.02,\ 0.69)$ nT and $[-0.73, -0.02)$ nT we see that the dayside scale values are higher than the nightside scale values throughout the time window. The nightside scale values decrease slightly before increasing again towards the end. Overall the scale values do not change drastically. For the negative intervals $[-1.51, -0.73)$ nT and $[-0.73, -0.02)$ nT the dayside and nightside scale values show a similar pattern. The dayside scale values initially overlap with the nightside scale before slightly increasing and decreasing again. The nightside scale values decrease before increasing again. In the $[-1.51, -0.73)$ nT interval, the nightside scale values surpass those of the dayside after 70 minutes. However, in the $[-0.73, -0.02)$ nT interval, the nightside scale does not surpass the dayside scale and instead overlaps with the dayside scale values at the very end of the interval. When comparing the scale values of the positive IMF Bz intervals $[0.69,\ 1.47)$ nT and $[-0.02,\ 0.69)$ nT with the negative intervals $[-1.51,\ -0.73)$ nT and $[-0.73,\ -0.02)$ nT, we observe that the values for the positive intervals are considerably higher than for the negative intervals. This discrepancy is largest for the stronger $[0.69,\ 1.47)$ nT and $[-1.51,\ -0.73)$ nT pairing.

Figure 5.10 shows the mean values of synthetic 50 000 reconnection rates generated using gamma distributions with the shape and scale parameter values shown in Figure 5.8 for the IMF Bz intervals $[0.69,\ 1.47)$ nT and $[-1.51,\ -0.73)$ nT, while Figure 5.11 shows those of the intervals $[-0.02,\ 0.69)$ nT and $[-0.73,\ -0.02)$ nT using the gamma parameters shown in Figure 5.9. For the predominantly positive IMF Bz intervals $[0.69,\ 1.47)$ nT and $[-0.02,\ 0.69)$ nT the means of the nightside reconnection rates are initially higher than the means of the dayside reconnection rates. The mean nightside reconnection rate for the $[0.69,\ 1.47)$ nT interval decreases steadily throughout the time window, whereas the mean rate for the $[-0.02,\ 0.69)$ interval decreases the first 65 minutes before increasing slightly. The mean dayside reconnection rate for the stronger interval $[0.69,\ 1.47)$ nT appears to increase linearly the entire time period and surpasses the mean nightside rate after 50 minutes. The mean dayside rate for the weaker interval $[-0.02,\ 0.69)$ nT also increases throughout the entire time period, albeit not as linearly, and crosses the mean nightside rate after 35 minutes. The mean dayside reconnection rate for both negative IMF Bz intervals $[-1.51,\ -0.73)$ nT and $[-0.73,\ -0.02)$ increases in the beginning of the time window before decreasing, while the mean nightside reconnection rate decreases in the beginning before increasing in the second half of the time period. In the $[-1.51,\ -0.73)$ nT interval the mean dayside is larger than the mean nightside rate until after 65 minutes, after which the mean nightside rate becomes bigger. In the $[-0.73,\ -0.02)$ nT interval the mean nightside rate is larger than the mean dayside rate the first 20 minutes. Comparing the positive IMF Bz intervals $[0.69,\ 1.47)$ nT and $[-0.02,\ 0.69)$ nT with the negative IMF Bz intervals $[-1.51,\ -0.73)$ nT and $[-0.73,\ -0.02)$ nT we observe that

the mean reconnection rate values are higher for the positive IMF Bz intervals. The mean reconnection rate values are within the range 16 kV to 20 kV for the positive [0.69, 1.47) nT interval compared to range 12.5 kV to 15 kV for the negative [−1.51, −0.73) nT interval, and the range 15 kV to 17.5 kV for the positive interval [−0.02, 0.69) nT compared to the range 14 kV and 16 kV for the negative [−0.73, −0.02) nT interval.

When comparing the mean synthetic reconnection rates to the mean of the actual reconnection rates, we see that the mean synthetic rates closely resemble the pattern of the mean of the actual rates. The time points at which the synthetic dayside and nightside mean reconnection rates intersect are the same as for the actual reconnection rates. The synthetic mean rates for the negative IMF Bz intervals are able to follow the actual rates more closely than their positive IMF Bz counterparts. However, the synthetic reconnection rates from the weaker IMF Bz intervals [−0.73, −0.02) nT and [−0.02, 0.69) nT deviate more from the actual rates than those generated within the stronger intervals.

5.4 Comparison of IMF Bz intervals

For the strongly and moderately positive IMF Bz intervals, we always observe that the mean nightside reconnection rate will dominate before the dayside reconnection rate eventually becomes bigger. The strongly and moderately negative IMF Bz intervals show the opposite and dayside reconnection rate is always larger before eventually the nightside rate becomes bigger. The reconnection rates in the positive IMF Bz intervals are also consistently higher than in the negative IMF Bz intervals, which is also reflected in the scale gamma parameter. These trends are the most distinct for stronger IMF Bz intervals. The nightside shape gamma parameter in the positive IMF Bz intervals is always initially larger than the dayside shape parameter, while the opposite is true for the negative IMF Bz intervals. A higher shape parameter indicates a bigger spread in values, while a lower shape parameter value indicates a sharper distribution with a lower mean value. This indicates that for the positive initial IMF Bz intervals, there is initially a larger spread in nightside reconnection rates and a smaller spread in dayside reconnection rates, with the opposite occurring for negative IMF Bz values.

All gamma distribution fits seem to fit reasonably well, but we see a larger relative error in gamma parameters for weak IMF Bz values in general. This is also reflected in the probability densities of the distributions compared to their respective gamma distribution fits. This subsequently leads to larger relative errors in the mean reconnection rates for the weaker IMF Bz intervals. The mean generated reconnection rates in these intervals are also not able to follow the actual reconnection rates as closely as the

rates generated for stronger IMF Bz values. It is also interesting to note that the means of the synthetic reconnection rates generated using an initial IMF Bz value within the positive intervals deviate more from the actual rates than their negative IMF Bz counterparts.

Chapter 6

Discussion

6.1 Obtaining the reconnection rates

There have been previous attempts at quantifying magnetic flux in the magnetosphere. One such approach, similar to the one used in this study developed by *Clausen et al.* [2013b], is the method proposed by *Hubert et al.* [2006]. The spectographic imager on the Imager for Magnetopause-to-Aurora Global Exploration (IMAGE) satellite was used to identify the location and movement of the OCB from the poleward edge of the main auroral oval, after which data from the Super Dual Aurora Network (SuperDARN) was used to determine the electric field at the location. Faraday's law was then used to obtain he amount of total open magnetic flux, similarly to what was done in our dataset. However, using this method they were only able to identify the OCB whenever the satellite was passing over the polar caps. With an orbital period of approximately 14 hours [*Hubert et al.*, 2006], it is not possible to find an estimate for the OCB, and subsequently open magnetic flux, for the full day. The accuracy of the estimated OCB using this method might fluctuate depending on the luminosity of the auroral oval, and could additionally be susceptible to daylight contamination *Hubert et al.* [2006]; *Shukhtina et al.* [2009]. An alternative approach to estimate the open magnetic flux was proposed by *Shukhtina et al.* [2009]. The open magnetic flux was estimated based on simultaneous solar wind and magnetotail measurements. The availability of such measurements is limited and the method is thus a less viable option to obtain the reconnection rates needed for the purpose of the study. Estimating the open magnetic flux from AMPERE data as derived by *Clausen et al.* [2013b], we assume that the OCB to be a clearly defined oval. However, looking at Figure 3.1, a well-defined oval is not immediately discernible. This is especially the case during quiet periods when there is little coupling between the IMF and the magnetosphere. Nevertheless, using the R1 oval to estimate the open magnetic flux is the most suitable for our purposes, as we are able to obtain

flux estimates at two-minute resolution with a larger and more consistent time coverage. Although the R1 oval is not necessarily easily discernible in absence of significant dayside and nightside reconnection, we are able to estimate the open magnetic flux from AMPERE data for every second minute of every day.

When combining the NH and SH magnetic flux, we used a weighted average based on which hemisphere had the strongest R1 current. We used the weights 0.3 and 0.7 respectively, with the hemisphere with the strongest current being weighted at 0.7 and the weakest being weighted at 0.3. It is possible that weighing directly based on R1 current strength would be a better approach, as *Clausen et al.* [2012] found that a stronger R1 current resulted in smaller errors. The weighted average then could have been constructed as

$$\overline{F}_{PC} = \frac{I_{NH}F_{NH} + I_{SH}F_{SH}}{I_{NH} + I_{SH}}, \tag{6.1}$$

where I_{NH}, F_{NH} are the R1 current and magnetic flux in the NH and I_{SH}, F_{SH} are the R1 current and magnetic flux in the SH and F_{PC} is the weighted average flux. However, there does not currently exist a standardised method to evaluate this method of combining the fluxes into a weighted average. From Figure 4.1 we see the open magnetic flux in the NH and in the SH do not deviate much from each other. suggesting that the weighting has most likely not lead to a significant change in results.

After filtering on IMF stability using the method developed by *Haaland et al.* [2007], we were left with approximately a third of the 1.8 million measurements, whereas the original authors were able to keep around half of their measurements. The method was based on setting a stability criterion for the direction of the IMF YZ vectors within a 30 minute interval. The discrepancy in retained measurements could be due to the difference in resolutions, as the original paper used measurements taken in 1 minute resolution compared to our resolution of 2 minutes. This means that for lower resolutions, random noise or rapid fluctuations in the IMF within the 30 minute intervals could have a larger impact on the overall stability of the IMF in the interval. Another reason could be that their IMF measurements were taken from 2001 to early 2006, which was during solar cycle 23, whereas our set was taken between 2010 and 2017 during solar cycle 24. It has been shown that IMF conditions vary with solar activity and solar cycle progression [e.g. *King*, 1979; *Gazis*, 1996]. Solar cycle 24 was a significantly quieter cycle compared to previous cycles [*Selvakumaran et al.*, 2016], which could have led to systematic differences in our datasets. Perhaps we could have experimented more with another threshold value in order to retain half of our measurements rather than one third. It could also be interesting to look at which IMF Bz measurements were filtered and their distribution compared to the distributions of the full dataset and the stable data. This way we could examine whether the stability criterion introduces a bias to-

wards certain values of the IMF and if maybe this could have affected the final observed distributions of the reconnection rates.

When deriving the dayside and nightside reconnection rates using Equation 2.1, due to having two unknowns and only one equation, we imposed that the dayside and nightside reconnection rates could never simultaneously be non-zero. This leads to the assumption that one reconnection rate is always strongly dominating while the other is zero and that it is not possible for dayside and nightside reconnection to occur at the same time. This is not a reflection of what happens in the magnetosphere in real life. There have been several attempts at parameterising the solar wind-magnetosphere coupling as so-called coupling functions [Table 2 in *Milan et al.*, 2012, and references therein]. These coupling functions are used to describe the coupling of energy between the IMF and the magnetosphere or the rate at which the IMF and the magnetosphere reconnect at the magnetopause [*Akasofu*, 1981], i.e. the dayside reconnection rate. Perhaps a better way for us to solve Equation 2.1 would be to use a proposed coupling function to quantify the dayside reconnection rate. The nightside reconnection rate could then have been derived directly from the equation by subtracting the open magnetic flux from the dayside rate. Our separation of the dayside and nightside rates leads to half of all the obtained reconnection rate values to be zero, even during strongly negative IMF Bz values that should lead to higher levels of solar wind-magnetosphere coupling. For future work it could be interesting to carry out the same research using a different method to derive the reconnection rates.

6.2 The derived reconnection rates and generated synthetic rates

Most of our obtained non-zero dayside and nightside reconnection rate values are within 0 kV and 100 kV, as seen from the distribution plots in Figure 5.1. This range is smaller than what has been modelled previously, e.g. *Hubert et al.* [2006] found that the nightside reconnection rate at substorm onset was typically over 100 kV and approximately between 30 kV and 40 kV during quiet periods. When smoothing the open magnetic flux change in order to obtain the reconnection rates, we used a rolling linear fit of 15 data points (30 minutes). We observe from Figure 4.2 that this led to significant smoothing of the flux change, effectively working as a low-pass filter. It is likely using a smaller smoothing interval would have left us with higher reconnection rate values.

We see from the mean of the obtained reconnection rates in Figure 5.3, Figure 5.6, Figure 5.7, Figure 5.10 and Figure 5.11 that, on average, the dayside reconnection rate dominates early on after an initial negative IMF Bz value. A negative initial IMF Bz value accompanied by a larger day-

side reconnection rate is consistent with the onset of the Dungey cycle [*Dungey*, 1961; *Arnoldy*, 1971], where we expect a southward IMF to trigger dayside reconnection. For the moderately and strongly negative IMF Bz intervals, the nightside shape value is initially smaller than the dayside shape. A lower shape value gives a more positively skewed distribution, meaning that the nightside reconnection rates are generally more concentrated around lower values, whereas the dayside reconnection rates are more spread. With the exception of the strongly negative IMF Bz interval, the scale values remain relatively stable throughout the time window for all negative intervals, indicating that the scaling of the reconnection rate values does not change much throughout the 90 minute interval. Over time we see that the dayside reconnection rate will diminish as the nightside reconnection rate increases and surpasses the dayside rate after $35 - 60$ minutes, which is consistent with what we expect from the shape and scale values. This corresponds well with previous observations that nightside reconnection does not occur immediately following dayside reconnection, but rather after a delay [*Siscoe and Huang*, 1985; *Cowley and Lockwood*, 1992]. *Beharrell and Honary* [2016] found that nightside reconnection occurs $60 - 120$ minutes after dayside reconnection. The start of our time window does not necessarily coincide with the onset of dayside reconnection which can explain why we observe that nightside reconnection surpasses dayside reconnection after only $35 - 60$ minutes. The IMF Bz likely becomes more positive over time and dayside reconnection subsides.

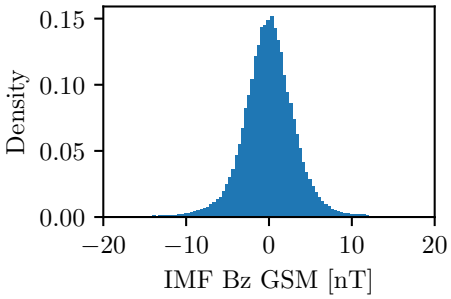

Figure 6.1: Distribution of IMF Bz values in the full dataset.

When the initial IMF Bz value is positive, we see a similar pattern as for a negative initial IMF Bz value, but reversed. The nightside reconnection on average dominates early on and the nightside shape is initially larger than the dayside shape until 50-60 minutes after the initial IMF Bz value. However, with the exception of the strongest magnetic field values, the negative IMF Bz intervals lead to weaker reconnection rates on average than their corresponding positive IMF Bz intervals. This is also reflected in the scale values, where the positive IMF Bz intervals have consistently higher values than their negative counterparts. This makes it unlikely that the time series of the positive intervals are a direct continuation of the time series of the negative intervals or vice versa. Another explanation could be that the IMF Bz has been negative for a longer period of time prior to the IMF Bz becoming positive. Figure 6.1 shows the distribution of the IMF Bz values

in our full dataset. The distribution is symmetrical around zero, making it reasonable to expect that the IMF Bz was negative before becoming positive. This could explain why the mean reconnection rates are higher for the initially positive IMF Bz values, as the magnetosphere has already reconfigured following a period of negative IMF Bz values. It could be interesting to look further into this offset between the mean reconnection rates following a positive or negative IMF Bz value. For the weak initial IMF Bz values, this pattern of alternate increase and decrease is prevalent in the weakly positive IMF Bz intervals, but not in the weakly negative intervals. Ionospheric activity is highly correlated with the magnitude of the IMF Bz strength [*Arnoldy*, 1971], which could explain why this pattern is not as distinct for the weak IMF Bz values. This can also provide an explanation as to why the weaker IMF Bz intervals lead to significantly lower mean reconnection rates.

Comparing the mean reconnection rate values with the distributions of the reconnection rates in Figure 5.1, it is clear that the mean values of the synthetic rates are lower than those of the distributions, which can be found as

$$\mu(k,\ \theta) = k\theta, \tag{6.2}$$

where $\mu(k,\ \theta)$ is the mean value of the distribution, k is the shape parameter and θ is the scale parameter. Taking e.g. the mean value of the nightside reconnection rate 0 minutes past an initial IMF Bz value within the [4.03, 37.70) nT interval, the mean value of the distribution and the synthetic rates is approximately 45 kV and 26 kV respectively. This is due to the zero values that were removed. As mentioned in section 6.1 it would be interesting to use a coupling parameter to derive the dayside and nightside reconnection rates to solve this issue.

6.3 Further use in ECPC

The synthetic reconnection rate at every time point in the series is either zero or randomly sampled from a distribution. This means that generating only one set of reconnection rates gives a highly discontinuous series of rates. Figure 6.2 shows one such series of synthetic dayside and nightside reconnection rates using an initial IMF Bz value of 5.0 nT, as well as the corresponding open magnetic flux change, cross polar cap potential (CPCP) and the open magnetic flux. The reconnection rate values at each time point are sampled independently without accounting for preceding values, which is evident in the figure, and physically interpreting one set of series is not possible. We observe that the open magnetic flux change and subsequent integrated open magnetic flux do not exhibit a distinct pattern associated with a positive IMF Bz value. However, generating more series of synthetic reconnection rates yields mean synthetic reconnection rates that are near

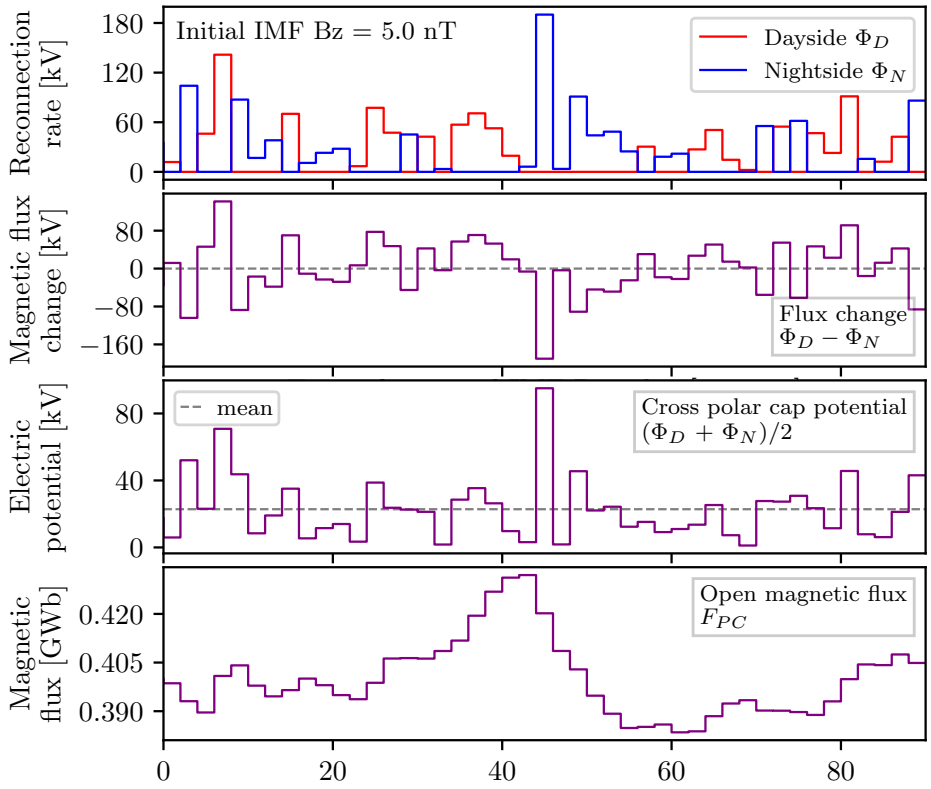

Figure 6.2: The upper plot shows one set of time series of synthetic dayside and nightside reconnection rates over 90 minutes using an initial IMF Bz value of 5.0 nT. The middle plots show the open magnetic flux change and the cross polar cap potential calculated according to Equation 2.3. The lower plot shows the open magnetic flux found by integrating the flux change using an initial value of 0.4 GWb.

identical to the means of the actual reconnection rates. The overall aim for these synthetic rates is to be used in an ECPC ensemble model based on previous work by *Fæhn Follestad et al.* [2019] for polar cap patch forecasting using instantaneous IMF measurements. By repeatedly running the model using a new set of synthetic reconnection rates, we can get a more statistical forecast of patch formation and propagation, as opposed to e.g. only using the mean reconnection rates.

The CPCP is calculated as the mean of the dayside reconnection rate and nightside reconnection rate according to Equation 2.3, consistent with the implementation of ECPC by *Fæhn Follestad et al.* [2019]. For this single set of synthetic reconnection rates as shown in Figure 6.2, the mean CPCP is slightly above 20 kV, with the maximum and minimum values being approximately 95 kV and 5 kV respectively. These are significantly

lower than the typical values obtained using SuperDARN for a strong IMF Bz value, with 20 kV being on the lower end of typical values [See Figure 4 in *Shepherd et al.*, 2002]. One reason could be that because the synthetic dayside and nightside rates are never simultaneously non-zero, the resulting CPCP is simply half the value of the non-zero rate. The IMF Bz interval that generates the highest synthetic reconnection rate values on average is the [4.03, 37.70) nT interval, with mean values ranging between 17 kV to 24 kV as seen in Figure 5.3, These low values subsequently result in low CPCP values using Equation 2.3 and very low activity levels in the ECPC model. However, Equation 2.2 from *Lockwood and Cowley* [1992] includes an additional term Φ_v arising from viscous-like interactions. *Fæhn Follestad et al.* [2019] use reconnection rates derived directly from SuperDARN CPCP values. The viscous-like term is included in these measurements and not separated from the dayside and nightside reconnection contributions. This suggests that it would be possible to add a positive offset to the synthetic reconnection rates in order to achieve activity levels that more accurately reflect the conditions in real life. This offset could be decided upon further experimentation.

We used gamma distributions to represent the distributions of the reconnection rates. Previous research has shown that many interplanetary space parameters and magnetospheric parameters closely follow log-normal distributions or other similar distributions [*Lockwood, Mike et al.*, 2018, and references therein]. *Lockwood, Mike et al.* [2018] state that a log-normal distribution can arise from multiplying individual parameters together. Previous attempts at quantifying the dayside reconnection rate as a coupling function indicate that the reconnection rate can be represented as a product of other space parameters, such as solar wind velocity and IMF strength [*Milan et al.*, 2012]. Additionally, gamma distributions are similar to log-normal distributions, making it is reasonable to assume that it would be possible to use log-normal distributions to represent the reconnection rates. It could prove useful to experiment further using log-normal distributions. Regardless, our method using gamma distributions has produced mean synthetic reconnection rates closely following the actual mean reconnection rates within reasonable relative errors. The relative error is larger for weaker IMF Bz values, which is consistent with what we expect of lower levels of ionospheric activity.

We have modelled series of dayside and nightside reconnection rates 90 minutes ahead of time given an initial IMF Bz value. Typical substorm lengths are between 1-4 hours [*Kullen and Karlsson*, 2004; *Tanskanen et al.*, 2011], with some substorms lasting longer. Our modelled time series of 90 minutes do not cover the full typical substorm duration. However, it is reasonable to assume that more series of rates can be generated following the initial 90 minutes for longer storms. This will likely lead to more accurate predictions, as our generated time series do not account for subsequent IMF

Bz values following the initially given value. It can be argued that producing even shorter time series using more instantaneous IMF Bz measurements could be beneficial.

As mentioned earlier, solar cycle 24, from which our measurements were taken, was significantly quieter than preceding cycles. *Partamies et al.* [2013] showed that substorm expansion and recovery phase lengths vary according to solar cycle progression. Because the IMF conditions vary with level of solar activity [*Gazis*, 1996], it could be beneficial to include additional measurements from previous solar cycles if this algorithm is to be used in forecasting polar cap prediction.

Chapter 7

Conclusion

In this study we have developed a method to generate 90-minute time series of synthetic reconnection rates, given an initial IMF Bz value, to be used in the ECPC ensemble model as implemented by *Fæhn Follestad et al.* [2019]. The synthetic reconnection rates were modelled on historical data of reconnection rates from the time period 05:00 UT 1st of January 2010 to 23:55 UT 31st of August 2017. The historical reconnection rates were estimated from the open magnetic flux derived from the R1 oval as described by *Clausen et al.* [2013b] using AMPERE data. The dayside and nightside reconnection rates were derived from the change in open magnetic by assuming that they can never simultaneously be non-zero. Our IMF Bz measurements were filtered on IMF stability according to the method described by *Haaland et al.* [2007], and divided into ten bins containing the same amount of measurements based on their value. For each IMF Bz value, we considered the dayside and nightside reconnection rates from the time the IMF measurement was taken to 90 minutes after. The distributions for the dayside and nightside reconnection rate were then estimated as gamma distributions given an initial IMF Bz value and a time point after the initial IMF Bz was measured. To generate one set of time series of synthetic rates given an IMF Bz value, the dayside and nightside rate values are chosen to be either zero or sampled from their corresponding gamma distributions, with the requirement that the dayside and nightside reconnection rates are never simultaneously non-zero.

Using this method to generate synthetic reconnection rates, for a sufficiently high number of synthetic reconnection rate series, we are able to almost perfectly replicate the mean of the reconnection rates derived using AMPERE data. The relative error in the means of the synthetic rates are smaller for strongly negative and strongly positive IMF Bz values and larger for weakly negative and weakly positive values. Given a negative initial IMF Bz value, we find that dayside reconnection dominates before diminishing and being overtaken by nightside reconnection, which is consistent

with what we expect of the Dungey cycle [e.g. *Cowley and Lockwood*, 1992]. For a positive initial IMF Bz value, the pattern is reversed and nightside reconnection dominates before eventually subsiding and being surpassed by dayside reconnection.

Both the dayside and nightside reconnection rates are shown to be higher for a positive initial IMF Bz value compared to a corresponding negative initial value. This could likely be due to the positive IMF Bz value following a prior period of negative IMF Bz values, such that the ionosphere is already reconfigured as a response to the external solar wind plasma.

7.1 Future work

When separating our dayside and nightside reconnection rates, we assumed that the dayside and nightside reconnection rates could never simultaneously be non-zero. This leads to a situation where constantly either dayside or nightside reconnection is dominating so that the other is zero. This in turn leads to generally lower values than what has been modelled previously, with half of all our values being zero and the other half falling between 0 kV to 100 kV. Using these synthetic reconnection rates directly in the ECPC model would likely not lead to any significant change in ionospheric activity. One solution to this could be to not make the assumption that dayside and nightside reconnection rates cannot occur at the same time, and instead use a coupling function to quantify the dayside reconnection rate and subtract the change in open magnetic flux to derive the nightside reconnection rate. Another solution could be to add an offset to the reconnection rate values, as the pattern for alternate increase and decrease in dayside and nightside reconnection still corresponds well with what we expect. Additionally, when deriving the change in open magnetic flux, we used a rolling linear fit on 30 minute intervals of flux to smoothen the data. This effectively led to higher reconnection rate values being filtered. Using a smaller interval would perhaps be beneficial to avoid strong smoothing of the higher values.

When applying these synthetic reconnection rates to the ECPC model to forecast future ionospheric convection patterns, it is important to note that these rates were derived from measurements taken during solar cycle 24, which was an unusually quiet year in relation to sunspot count [*Selvakumaran et al.*, 2016]. It could prove beneficial to apply this method to a larger quantity of data taken from e.g. solar cycle 23, which had noticeably more activity than solar cycle 24.

Bibliography

Aarons, J., The longitudinal morphology of equatorial F-layer irregularities relevant to their occurrence, *Space Science Reviews*, *63*(3-4), 209–243, 1993.

Akasofu, S.-I., Energy coupling between the solar wind and the magnetosphere, *Space Science Reviews*, *28*(2), 121–190, doi:https://doi.org/10.1007/BF00218810, 1981.

Anderson, B. J., K. Takahashi, and B. A. Toth, Sensing global Birkeland currents with Iridium® engineering magnetometer data, *Geophysical Research Letters*, *27*(24), 4045–4048, doi:https://doi.org/10.1029/2000GL000094, 2000.

Anderson, B. J., H. Korth, C. L. Waters, D. L. Green, V. G. Merkin, R. J. Barnes, and L. P. Dyrud, Development of large-scale Birkeland currents determined from the Active Magnetosphere and Planetary Electrodynamics Response Experiment, *Geophysical Research Letters*, *41*(9), 3017–3025, doi:https://doi.org/10.1002/2014GL059941, 2014.

Arnoldy, R. L., Signature in the interplanetary medium for substorms, *Journal of Geophysical Research (1896-1977)*, *76*(22), 5189–5201, doi:https://doi.org/10.1029/JA076i022p05189, 1971.

Basu, S., E. MacKenzie, and S. Basu, Ionospheric constraints on vhf/uhf communications links during solar maximum and minimum periods, *Radio Science*, *23*(3), 363–378, doi:https://doi.org/10.1029/RS023i003p00363, 1988.

Beharrell, M. J., and F. Honary, Decoding solar wind-magnetosphere coupling, *Space Weather*, *14*(10), 724–741, doi:https://doi.org/10.1002/2016SW001467, 2016.

Bristow, W. A., R. A. Greenwald, S. G. Shepherd, and J. M. Hughes, On the observed variability of the cross–polar cap potential, *Journal of Geophysical Research: Space Physics*, *109*(A2), doi:https://doi.org/10.1029/2003JA010206, 2004.

Clausen, L. B. N., J. B. H. Baker, J. M. Ruohoniemi, S. E. Milan, and B. J. Anderson, Dynamics of the region 1 Birkeland current oval derived from the Active Magnetosphere and Planetary Electrodynamics Response Experiment (AMPERE), *Journal of Geophysical Research: Space Physics*, *117*(A6), doi:https://doi.org/10.1029/2012JA017666, 2012.

Clausen, L. B. N., J. B. H. Baker, J. M. Ruohoniemi, S. E. Milan, J. C. Coxon, S. Wing, S. Ohtani, and B. J. Anderson, Temporal and spatial dynamics of the regions 1 and 2 Birkeland currents during substorms, *Journal of Geophysical Research: Space Physics*, *118*(6), 3007–3016, doi:https://doi.org/10.1002/jgra.50288, 2013a.

Clausen, L. B. N., S. E. Milan, J. B. H. Baker, J. M. Ruohoniemi, K.-H. Glassmeier, J. C. Coxon, and B. J. Anderson, On the influence of open magnetic flux on substorm intensity: Ground- and space-based observations, *Journal of Geophysical Research: Space Physics*, *118*(6), 2958–2969, doi:https://doi.org/10.1002/jgra.50308, 2013b.

Cowley, S., Magnetosphere-ionosphere interactions: A Tutorial Review, *Magnetospheric Current Systems, Geophys. Monogr. Ser*, *118*, 91–106, doi:https://doi.org/10.1029/GM118p0091, 2000.

Cowley, S., and M. Lockwood, Excitation and decay of solar wind-driven flows in the magnetosphere-ionosphere system, *Annales Geophysicae*, *10*(1-2), 103–115, 1992.

Coxon, J. C., S. E. Milan, L. B. N. Clausen, B. J. Anderson, and H. Korth, The magnitudes of the regions 1 and 2 birkeland currents observed by ampere and their role in solar wind-magnetosphere-ionosphere coupling, *Journal of Geophysical Research: Space Physics*, *119*(12), 9804–9815, doi:https://doi.org/10.1002/2014JA020138, 2014.

Coxon, J. C., S. E. Milan, and B. J. Anderson, *A Review of Birkeland Current Research Using AMPERE*, chap. 16, pp. 257–278, American Geophysical Union (AGU), doi:https://doi.org/10.1002/9781119324522.ch16, 2018.

Crowley, G., Critical review of ionospheric patches and blobs, *Review of Radio Science 1993–1996*, pp. 619–648, 1996.

Crowley, G., et al., Transformation of high-latitude ionospheric f region patches into blobs during the march 21, 1990, storm, *Journal of Geophysical Research: Space Physics*, *105*(A3), 5215–5230, doi:https://doi.org/10.1029/1999JA900357, 2000.

Dungey, J. W., Interplanetary Magnetic Field and the Auroral Zones, *Phys. Rev. Lett.*, *6*, 47–48, doi:https://doi.org/10.1103/PhysRevLett.6.47, 1961.

Freeman, M. P., A unified model of the response of ionospheric convection to changes in the interplanetary magnetic field, *Journal of Geophysical Research: Space Physics*, *108*(A1), SMP 14–1–SMP 14–13, doi:https://doi.org/10.1029/2002JA009385, 2003.

Fremouw, E. J., R. L. Leadabrand, R. C. Livingston, M. D. Cousins, C. L. Rino, B. C. Fair, and R. A. Long, Early results from the dna wideband satellite experiment—complex-signal scintillation, *Radio Science*, *13*(1), 167–187, doi:https://doi.org/10.1029/RS013i001p00167, 1978.

Fæhn Follestad, A., L. B. N. Clausen, E. G. Thomas, Y. Jin, and A. Coster, Polar Cap Patch Prediction in the Expanding Contracting Polar Cap Paradigm, *Space Weather*, *17*(11), 1570–1583, doi:https://doi.org/10.1029/2019SW002276, 2019.

Gao, Y., Comparing the cross polar cap potentials measured by superdarn and amie during saturation intervals, *Journal of Geophysical Research: Space Physics*, *117*(A8), doi:https://doi.org/10.1029/2012JA017690, 2012.

Gazis, P. R., Solar cycle variation in the heliosphere, *Reviews of Geophysics*, *34*(3), 379–402, doi:https://doi.org/10.1029/96RG00892, 1996.

Gold, T., Plasma and magnetic fields in the solar system, *Journal of Geophysical Research (1896-1977)*, *64*(11), 1665–1674, doi:https://doi.org/10.1029/JZ064i011p01665, 1959.

Haaland, S. E., G. Paschmann, M. Förster, J. M. Quinn, R. B. Torbert, C. E. McIlwain, H. Vaith, P. A. Puhl-Quinn, and C. A. Kletzing, High-latitude plasma convection from Cluster EDI measurements: method and IMF-dependence, *Annales Geophysicae*, *25*(1), 239–253, doi:https://doi.org/10.5194/angeo-25-239-2007, 2007.

Hubert, B., S. E. Milan, A. Grocott, C. Blockx, S. W. H. Cowley, and J.-C. Gérard, Dayside and nightside reconnection rates inferred from IMAGE FUV and Super Dual Auroral Radar Network data, *Journal of Geophysical Research: Space Physics*, *111*(A3), doi:https://doi.org/10.1029/2005JA011140, 2006.

Iijima, T., and T. A. Potemra, The amplitude distribution of field-aligned currents at northern high latitudes observed by triad, *Journal of Geophysical Research (1896-1977)*, *81*(13), 2165–2174, doi:https://doi.org/10.1029/JA081i013p02165, 1976.

Iijima, T., and T. A. Potemra, Large-scale characteristics of field-aligned currents associated with substorms, *Journal of Geophysical Research: Space Physics*, *83*(A2), 599–615, doi:https://doi.org/10.1029/JA083iA02p00599, 1978.

Jin, Y., J. Moen, and W. Miloch, GPS scintillation effects associated with polar cap patches and substorm auroral activity: Direct comparison, *Journal of Space Weather and Space Climate*, *4*, A23, doi:https://doi.org/10.1051/swsc/2014019, 2014.

Jin, Y., J. I. Moen, and W. J. Miloch, On the collocation of the cusp aurora and the gps phase scintillation: A statistical study, *Journal of Geophysical Research: Space Physics*, *120*(10), 9176–9191, doi:https://doi.org/10.1002/2015JA021449, 2015.

Jin, Y., J. I. Moen, W. J. Miloch, L. B. N. Clausen, and K. Oksavik, Statistical study of the gnss phase scintillation associated with two types of auroral blobs, *Journal of Geophysical Research: Space Physics*, *121*(5), 4679–4697, doi:https://doi.org/10.1002/2016JA022613, 2016.

Kamide, Y., W. Sun, and S.-I. Akasofu, The average ionospheric electrodynamics for the different substorm phases, *Journal of Geophysical Research: Space Physics*, *101*(A1), 99–109, doi:https://doi.org/10.1029/95JA02990, 1996.

King, J. H., Solar cycle variations in IMF intensity, *Journal of Geophysical Research: Space Physics*, *84*(A10), 5938–5940, doi:https://doi.org/10.1029/JA084iA10p05938, 1979.

King, J. H., and N. E. Papitashvili, Solar wind spatial scales in and comparisons of hourly Wind and ACE plasma and magnetic field data, *Journal of Geophysical Research: Space Physics*, *110*(A2), doi:https://doi.org/10.1029/2004JA010649, 2005.

Korth, H., B. J. Anderson, and C. L. Waters, Statistical analysis of the dependence of large-scale Birkeland currents on solar wind parameters, *Annales Geophysicae*, *28*(2), 515–530, doi:https://doi.org/10.5194/angeo-28-515-2010, 2010.

Kullen, A., and T. Karlsson, On the relation between solar wind, pseudobreakups, and substorms, *Journal of Geophysical Research: Space Physics*, *109*(A12), doi:https://doi.org/10.1029/2004JA010488, 2004.

Lockwood, M., and S. Cowley, *Ionospheric convection and the substorm cycle, in: Proceedings of the Inturnal of Geophysical Reernational Conference on Substorms (ICS-1)*, pp. 99–109, European Space Agency Publications, Nordvijk, The Netherlands, 1992.

Lockwood, Mike, Owens, Mathew J., Barnard, Luke A., Scott, Chris J., Watt, Clare E., and Bentley, Sarah, Space climate and space weather over the past 400rs: 2. Proxy indicators of geomagnetic storm and substorm occurrence, *J. Space Weather Space Clim.*, *8*, A12, doi:10.1051/swsc/2017048, 2018.

McPherron, R. L., C. T. Russell, and M. P. Aubry, Satellite studies of magnetospheric substorms on august 15, 1968: 9. phenomenological model for substorms, *Journal of Geophysical Research (1896-1977)*, *78*(16), 3131–3149, doi:https://doi.org/10.1029/JA078i016p03131, 1973.

Milan, S. E., Modeling Birkeland currents in the expanding/contracting polar cap paradigm, *Journal of Geophysical Research: Space Physics*, *118*(9), 5532–5542, doi:https://doi.org/10.1002/jgra.50393, 2013.

Milan, S. E., J. S. Gosling, and B. Hubert, Relationship between interplanetary parameters and the magnetopause reconnection rate quantified from observations of the expanding polar cap, *Journal of Geophysical Research: Space Physics*, *117*(A3), doi:https://doi.org/10.1029/2011JA017082, 2012.

Moukarzel, J., From Scratch: Bayesian Inference, Markov Chain Monte Carlo and Metropolis Hastings, in python, url: https://towardsdatascience.com/from-scratch-bayesian-inference-markov-chain-monte-carlo-and-metropolis-hastings-in-python-ef21a29e25a (accessed: 27.04.2021), 2018.

Oksavik, K., V. L. Barth, J. Moen, and M. Lester, On the entry and transit of high-density plasma across the polar cap, *Journal of Geophysical Research: Space Physics*, *115*(A12), doi:https://doi.org/10.1029/2010JA015817, 2010.

Owens, M. J., and R. J. Forsyth, The Heliospheric Magnetic Field, *Living Reviews in Solar Physics*, *10*(1), 1–52, 2013.

Partamies, N., L. Juusola, E. Tanskanen, and K. Kauristie, Statistical properties of substorms during different storm and solar cycle phases, *Annales Geophysicae*, *31*(2), 349–358, doi:https://doi.org/10.5194/angeo-31-349-2013, 2013.

Prikryl, P., P. T. Jayachandran, S. C. Mushini, and R. Chadwick, Climatology of gps phase scintillation and hf radar backscatter for the high-latitude ionosphere under solar minimum conditions, *Annales Geophysicae*, *29*(2), 377–392, doi:10.5194/angeo-29-377-2011, 2011.

Ridley, A. J., G. Lu, C. R. Clauer, and V. O. Papitashvili, A statistical study of the ionospheric convection response to changing interplanetary magnetic field conditions using the assimilative mapping of ionospheric electrodynamics technique, *Journal of Geophysical Research: Space Physics*, *103*(A3), 4023–4039, doi:https://doi.org/10.1029/97JA03328, 1998.

Ruanaidh, J. J. O., and W. J. Fitzgerald, *Numerical Bayesian methods applied to signal processing*, 78–81 pp., Springer Science & Business Media, doi:https://doi.org/10.1007/978-1-4612-0717-7, 1996.

Russell, C. T., The configuration of the magnetosphere, in *Critical problems of magnetospheric physics*, edited by E. Dyer, pp. 1–16, Washington, DC: National Academy of Sciences, 1972.

Russell, C. T., J. G. Luhmann, and R. J. Strangeway, *Space physics: An introduction*, 290, 315–321 pp., Cambridge University Press, 2016.

Selvakumaran, R., B. Veenadhari, S. Akiyama, M. Pandya, N. Gopalswamy, S. Yashiro, S. Kumar, P. Mäkelä, and H. Xie, On the reduced geoeffectiveness of solar cycle 24: A moderate storm perspective, *Journal of Geophysical Research: Space Physics*, *121*(9), 8188–8202, doi: https://doi.org/10.1002/2016JA022885, 2016.

Shepherd, S. G., and J. M. Ruohoniemi, Electrostatic potential patterns in the high-latitude ionosphere constrained by superdarn measurements, *Journal of Geophysical Research: Space Physics*, *105*(A10), 23,005–23,014, doi:https://doi.org/10.1029/2000JA000171, 2000.

Shepherd, S. G., R. A. Greenwald, and J. M. Ruohoniemi, Cross polar cap potentials measured with super dual auroral radar network during quasi-steady solar wind and interplanetary magnetic field conditions, *Journal of Geophysical Research: Space Physics*, *107*(A7), SMP 5–1–SMP 5–11, doi:https://doi.org/10.1029/2001JA000152, 2002.

Shukhtina, M. A., E. I. Gordeev, and V. A. Sergeev, Time-varying magnetotail magnetic flux calculation: a test of the method, *Annales Geophysicae*, *27*(4), 1583–1591, doi:https://doi.org/10.5194/angeo-27-1583-2009, 2009.

Siscoe, G. L., and T. S. Huang, Polar cap inflation and deflation, *Journal of Geophysical Research: Space Physics*, *90*(A1), 543–547, doi:https://doi.org/10.1029/JA090iA01p00543, 1985.

Spogli, L., L. Alfonsi, G. De Franceschi, V. Romano, M. H. O. Aquino, and A. Dodson, Climatology of gps ionospheric scintillations over high and mid-latitude european regions, *Annales Geophysicae*, *27*(9), 3429–3437, doi:10.5194/angeo-27-3429-2009, 2009.

Tanskanen, E. I., T. I. Pulkkinen, A. Viljanen, K. Mursula, N. Partamies, and J. A. Slavin, From space weather toward space climate time scales: Substorm analysis from 1993 to 2008, *Journal of Geophysical Research: Space Physics*, *116*(A5), doi:https://doi.org/10.1029/2010JA015788, 2011.

Walach, M.-T., S. E. Milan, T. K. Yeoman, B. A. Hubert, and M. R. Hairston, Testing nowcasts of the ionospheric convection from the expanding and contracting polar cap model, *Space Weather*, *15*(4), 623–636, doi:https://doi.org/10.1002/2017SW001615, 2017.

Waters, C. L., B. J. Anderson, and K. Liou, Estimation of global field aligned currents using the iridium® System magnetometer data, *Geophysical Research Letters*, *28*(11), 2165–2168, doi:https://doi.org/10.1029/2000GL012725, 2001.

Weber, E. J., J. Buchau, J. G. Moore, J. R. Sharber, R. C. Livingston, J. D. Winningham, and B. W. Reinisch, F layer ionization patches in the polar cap, *Journal of Geophysical Research: Space Physics*, *89*(A3), 1683–1694, doi:https://doi.org/10.1029/JA089iA03p01683, 1984.

Zhang, Q.-H., et al., On the importance of interplanetary magnetic field —By— on polar cap patch formation, *Journal of Geophysical Research: Space Physics*, *116*(A5), doi:https://doi.org/10.1029/2010JA016287, 2011.